AGU PUBLICATIONS

JGR

Journal of Geophysical Research: Space Physics

RESEARCH ARTICLE

10.1002/2014JA020373

Special Section:
New perspectives on Earth's radiation belt regions from the prime mission of the Van Allen Probes

Key Points:

- The Van Allen Probes observed ULF waves in the plasmasphere
- The waves were driven by ULF waves in the foreshock region
- Plasmaspheric mass density is estimated from the frequency of the waves

Correspondence to:
K. Takahashi,
kazue.takahashi@jhuapl.edu

Citation:
Takahashi, K., R. E. Denton, W. Kurth, C. Kletzing, J. Wygant, J. Bonnell, L. Dai, K. Min, C. W. Smith, and R. MacDowall (2015), Externally driven plasmaspheric ULF waves observed by the Van Allen Probes, *J. Geophys. Res. Space Physics*, *120*, 526–552, doi:10.1002/2014JA020373.

Received 7 JUL 2014
Accepted 13 DEC 2014
Accepted article online 22 DEC 2014
Published online 30 JAN 2015

Externally driven plasmaspheric ULF waves observed by the Van Allen Probes

Kazue Takahashi[1], Richard E. Denton[2], William Kurth[3], Craig Kletzing[3], John Wygant[4], John Bonnell[5], Lei Dai[4], Kyungguk Min[6], Charles W. Smith[7], and Robert MacDowall[8]

[1]Johns Hopkins University Applied Physics Laboratory, Laurel, Maryland, USA, [2]Department of Physics and Astronomy, Dartmouth College, Hanover, New Hampshire, USA, [3]Department of Physics and Astronomy, University of Iowa, Iowa City, Iowa, USA, [4]School of Physics and Astronomy, University of Minnesota, Twin Cities, Minneapolis, Minnesota, USA, [5]Space Sciences Laboratory, University of California, Berkeley, California, USA, [6]Department of Physics, Auburn University, Auburn, Alabama, USA, [7]Department of Physics and Institute for the Study of Earth, Oceans and Space, University of New Hampshire, Durham, New Hampshire, USA, [8]Solar System Exploration Division, Goddard Space Flight Center, Greenbelt, Maryland, USA

Abstract We analyze data acquired by the Van Allen Probes on 8 November 2012, during a period of extended low geomagnetic activity, to gain new insight into plasmaspheric ultralow frequency (ULF) waves. The waves exhibited strong spectral power in the 5–40 mHz band and included multiharmonic toroidal waves visible up to the eleventh harmonic, unprecedented in the plasmasphere. During this wave activity, the interplanetary magnetic field cone angle was small, suggesting that the waves were driven by broadband compressional ULF waves originating in the foreshock region. This source mechanism is supported by the tailward propagation of the compressional magnetic field perturbations at a phase velocity of a few hundred kilometers per second that is determined by the cross-phase analysis of data from the two spacecraft. We also find that the coherence and phase delay of the azimuthal components of the magnetic field from the two spacecraft strongly depend on the radial separation of the spacecraft and attribute this feature to field line resonance effects. Finally, using the observed toroidal wave frequencies, we estimate the plasma mass density for $L = 2.6$–5.8. By comparing the mass density with the electron number density that is estimated from the spectrum of plasma waves, we infer that the plasma was dominated by H^+ ions and was distributed uniformly along the magnetic field lines. The electron density is higher than the prediction of saturated plasmasphere models, and this "super saturated" plasmasphere and the uniform ion distribution are consistent with the low geomagnetic activity that prevailed.

1. Introduction

Ground magnetometers located at plasmaspheric latitudes routinely detect dayside ultralow frequency (ULF) pulsations in the Pc3–Pc5 band (2–100 mHz). The pulsations have been attributed to magnetospheric magnetohydrodynamic (MHD) waves including fast mode waves [e.g., *Vellante et al.*, 1996] and toroidal standing Alfvén waves (field line resonances) [e.g., *Waters et al.*, 1991]. The MHD waves are likely driven by source mechanisms external to the magnetosphere, such as solar wind dynamic pressure variations [e.g., *Villante et al.*, 2007], ULF waves generated in the foreshock region [e.g., *Troitskaya*, 1994], and the Kelvin-Helmholtz instability on the magnetopause [*Wolfe et al.*, 1980]. Because ULF waves detected on the ground are modified by the ionosphere [e.g., *Pilipenko et al.*, 2000], it is necessary to observe the waves in the magnetosphere to understand their physical properties more precisely.

Currently, there is much need to determine the properties of plasmaspheric ULF waves in relation to the behavior of energetic particles in the outer zone radiation belt and ring current ($L = 2$–7) [*Mauk et al.*, 2013]. Information we need on the waves includes polarization, spectral intensity, spatial mode structure, and propagation direction. The information is essential, for example, when one evaluates the efficiency of radial diffusion [e.g., *Brautigam et al.*, 2005] or examines the validity of simulated ULF wavefields that change particle orbit and energy [e.g., *Fei et al.*, 2006; *Degeling et al.*, 2011].

Until now, in situ observations of plasmaspheric ULF waves have been limited. For example, although statistical studies have been conducted using magnetic field data from both the equatorially orbiting Active Magnetospheric Particle Tracer Explorers Charge Composition Explorer (AMPTE/CCE) spacecraft [*Takahashi* *and Anderson*, 1992] and the polar-orbiting Challenging Minisatellite Payload (CHAMP) spacecraft [*Heilig et al.*, 2007], the lack of electric field measurements on these spacecraft makes it difficult to discuss the modes of the waves. The better equipped Time History of Events and Macroscale Interactions during Substorms (THEMIS) spacecraft traverse the equatorial plasmasphere and detect trapped fast mode waves and toroidal standing Alfvén waves [*Takahashi et al.*, 2010a], as well as internally excited poloidal standing Alfvén waves [*Liu et al.*, 2013]. However, because the THEMIS spacecraft spend a small amount of time in the plasmasphere, they are not ideal for studying plasmaspheric phenomena. The Combined Release and Radiation Effects Satellite (CRRES) spacecraft was ideal in both instrumentation and orbital configuration, but the early termination of its science operation left a very limited temporal coverage and a dayside void in spatial coverage [*Takahashi et al.*, 2004].

In addition, much remains to be done regarding plasma mass density diagnostics using ULF waves (magnetoseismology) in the plasmasphere. ULF waves observed on the ground have been extensively used to monitor plasmaspheric mass density [*Chi et al.*, 2005; *Dent et al.*, 2006; *Menk and Waters*, 2013]. With spacecraft observations, we have the advantage of having electron density measurements, which give us information on the ion composition when combined with the mass density estimated using magnetoseismic techniques [*Denton*, 2006]. This advantage was obvious in CRRES studies [*Takahashi et al.*, 2004, 2008]. It is desirable that the magnetoseismic technique is applied to data from other spacecraft to cover magnetospheric regions and geomagnetic conditions that were not covered by CRRES.

The recently launched Van Allen Probes [*Mauk et al.*, 2013] provide us with an opportunity to significantly improve our understanding of the physical properties of plasmaspheric ULF waves and their relation to the mass density. In this paper, we show an example of ULF waves in the 5–40 mHz frequency range (part of the Pc3–Pc5 pulsation band) observed from the Van Allen Probes, describe their propagation mode and source mechanism, and use the spectral information from the waves to infer the mass density and ion composition.

The present paper includes the following results. First, we present evidence that broadband compressional waves originating in the Earth's foreshock region excited toroidal standing Alfvén waves at the fundamental through the eleventh harmonic, with the power mostly contained in the odd harmonics. This is the first time that multiharmonic toroidal waves in the plasmasphere were observed up to such high-order harmonics. Second, we examine the phase delay of compressional and azimuthal oscillations of the magnetic field between the two spacecraft and interpret the result in terms of fast mode propagation and field line resonance effects. This is made possible by the unique orbital configuration of the Van Allen Probes. Third, we use the toroidal wave frequencies to estimate the plasma mass density and compare it with the electron number density determined from plasma wave spectra. The long residence times of the Van Allen Probes in the plasmasphere allow us to gain more detailed information on the mass density that was possible with other spacecraft.

The remainder of the paper is organized as follows. Section 2 describes the experiments. Section 3 presents the spectral properties of the waves. Section 4 describes the solar wind condition and discusses the wave generation mechanism. Section 5 examines the phase delay of magnetic field oscillations between the two Van Allen probes. Section 6 presents mass density analysis. Section 7 presents the summary, and Section 8 concludes the study.

2. Orbit Configuration and Experiments

The Van Allen Probes were launched on 30 August 2012 into elliptical orbits with perigee distance of 1.1 R_E (geocentric), apogee distance of 5.8 R_E, inclination of 10°, and orbital period of ∼9 h. The spacecraft are spin stabilized with the spin axis approximately pointing to the Sun and a spin period of ∼11 s. Figure 1 shows the orbit of Van Allen Probe A on which the ULF waves studied in this paper were observed. The orbit is plotted using the dipole L as the radius and the longitude in the solar magnetospheric (SM) coordinate system (ϕ_{SM}) as the azimuth. The apogee was located at ∼0600 magnetic local time (MLT), so the outbound and inbound legs occurred in the postmidnight and prenoon sectors, respectively. Van Allen Probe B was on a nearly identical orbit but reached its apogee 5 min ahead of Van Allen Probe A.

Figure 2 shows the positions of both spacecraft in dipole-based coordinates: L, magnetic latitude (MLAT), and MLT. The spacecraft were close to each other in all these coordinates (Figures 2a–2c), and it is important to note that the spacecraft were close to the magnetic equator ($|\text{MLAT}| < 5°$) except near the perigees.

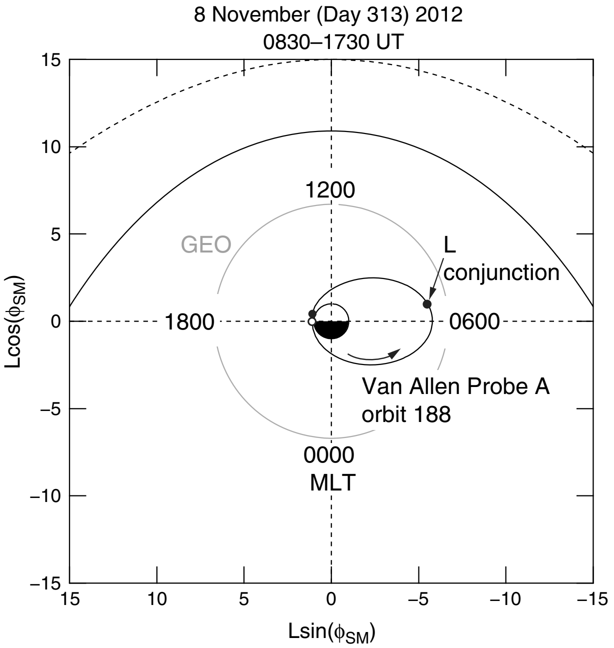

Figure 1. Location of Van Allen Probe A on orbit 188, which spanned 0830–1730 UT on 8 November 2012. In this plot, the radius is the dipole L and the azimuth (ϕ_{SM}) is the longitude in the SM coordinates. Model magnetopause (outer solid black curve) and bow shock (dashed black curve) and geostationary orbit (GEO, solid gray curve) are included for reference. An L conjunction with Van Allen Probe B occurred near dawn.

Figures 2d–2f show the separation of the spacecraft, which is defined to be the position of Van Allen Probe B relative to Van Allen Probe A (e.g., $\Delta L = L_{\mathrm{B}} - L_{\mathrm{A}}$). Key features to be noted in the main part of the orbits, 1000–1600 universal time (UT), are the following: (1) Van Allen Probe A was at lower L until the L conjunction at 1351 UT. (2) Separation in MLAT was less than 1°. (3) Van Allen Probe A was located at earlier MLT, with separation less than 0.3 h for $L \geq 3$.

Data used in this study were acquired with two experiments onboard each of the Van Allen Probes: the Electric and Magnetic Field Instrument Suite and Integrated Science (EMFISIS) [*Kletzing et al.*, 2013] and the Electric Field and Waves (EFW) instruments [*Wygant et al.*, 2013]. EMFISIS includes a fluxgate magnetometer and an electric field spectrum analyzer. The magnetometer measures the magnetic field (denoted **B**) with the sampling rate of 64 vector/s. Under the normal operation, the magnetometer switches between the two dynamic ranges, Range 1 (−4096 to 4096 nT, resolution 0.125 nT) and Range 3 (−65536 to 65536 nT, resolution 2 nT). We use fluxgate magnetometer data that are provided in 1 s resolution. We take 11 s running averages of the data to suppress the 11 s spin modulation. The relative timing of the magnetometer data from the two spacecraft has accuracy no worse than ±0.1 s. The spectrum analyzer provides a power spectrum over the 10–400 kHz frequency band every 6 s. Data from the spectrum analyzer are used to determine the electron number density, n_{e}, based on the relationship between the density and characteristic frequencies in the spectrum: the plasma frequency cutoff of continuum radiation and the upper hybrid resonance. The ultimate accuracy of n_{e} is given by $\Delta n_{\mathrm{e}}/n_e = 10\%$, directly related to the spectral resolution, 5%, of the plasma wave experiment. On the orbits examined here, the upper hybrid band is very clear, and the estimated density probably has an accuracy close to 10%. EFW measures the electric field (denoted **E**) with the sampling rate of 32 vectors/s. We use electric field measured in the spacecraft spin plane and reduced to ∼11 s time resolution by the spin-fit procedure described by *Wygant et al.* [2013].

We use two coordinate systems for **E** and **B**. In one system, called the magnetic field-aligned (MFA) coordinates, the compressional component $\mathbf{e}_\mu$ is along the magnetic field given by combining the International Geomagnetic Reference Field (http://www.ngdc.noaa.gov/IAGA) and the T89c model field [*Tsyganenko*, 1989]; the eastward component $\mathbf{e}_\phi$ is in the direction of $\mathbf{e}_\mu \times \mathbf{R}$, where **R** is the radial vector pointing from the center of the Earth toward the satellite; and the radial component $\mathbf{e}_\nu$ completes the right-handed system ν-ϕ-μ. This system is used to separate magnetic field perturbations into the poloidal, toroidal, and compressional components. For the time series analysis of the magnetic field, we subtract the magnitude of the model magnetic field from the B_μ component. In the other system, called the modified geocentric solar ecliptic (MGSE) coordinates, the x axis ($\mathbf{e}_{x\mathrm{MGSE}}$, pointing sunward) is parallel to the spacecraft spin axis, which is maintained within ∼20° of the Sun-Earth line, the y axis ($\mathbf{e}_{y\mathrm{MGSE}}$, pointing duskward) is along $\mathbf{e}_{z\mathrm{GSE}} \times \mathbf{e}_{x\mathrm{MGSE}}$, where $\mathbf{e}_{z\mathrm{GSE}}$ is the z axis of the GSE coordinates, and the z axis ($\mathbf{e}_{z\mathrm{MGSE}}$, pointing northward) is along $\mathbf{e}_{x\mathrm{MGSE}} \times \mathbf{e}_{y\mathrm{MGSE}}$. This system is used to express the two components of the electric field vectors measured in the satellite spin plane. The third component of the electric field could be obtained

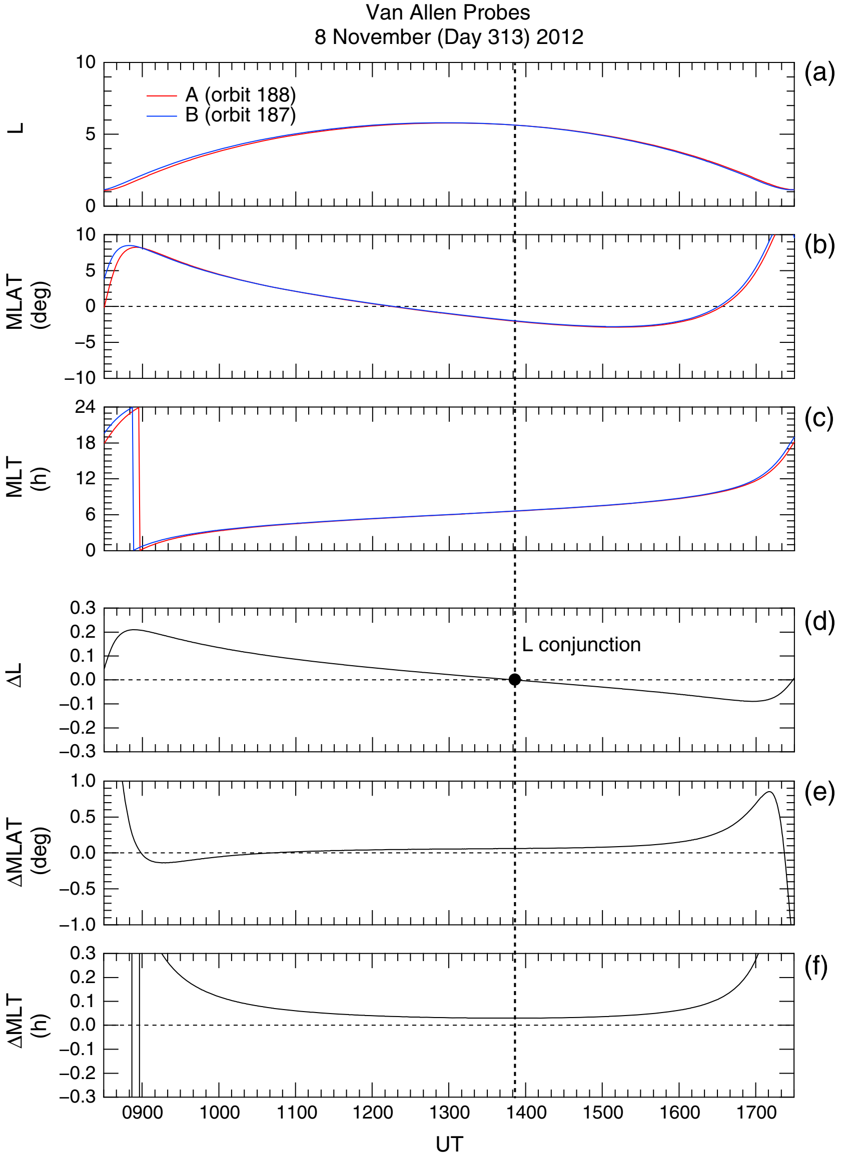

Figure 2. (a–c) Position of the Van Allen Probes in the dipole-based *L*, MLAT, and MLT coordinates. (d–f) Separation of the spacecraft in the same coordinates. The separation is defined to be the position of Van Allen Probe B relative to Van Allen Probe A, e.g., $\Delta L = L_B - L_A$. The vertical dashed line indicates the *L* conjunction at 1351 UT.

by using the $\mathbf{E}\cdot\mathbf{B} = 0$ assumption [e.g., *Dai et al.*, 2013], but this technique is not used in the present study because of the unfavorable orientation of the spin plane relative to the ambient magnetic field.

3. Spectral Properties of the Waves

3.1. Dynamic Spectra

Figure 3 provides an overview of the ULF wave activity at Van Allen Probe A on the selected orbit. The spacecraft position is shown at the bottom using dipole-based coordinates. We have included the magnetic field magnitude (Figure 3a) and electron number density (Figure 3b) to provide information on the background magnetic field and plasma. The electron density varies smoothly to the minimum value of 150 cm^{-3}, seen at 1240 UT (near apogee) inside a small dip, suggesting that the spacecraft might have briefly entered a plasmapause density gradient. However, this density is well above the typical plasma trough density at $L \sim 6$ (below ∼10 cm^{-3}) [*Carpenter and Anderson*, 1992], which means that the spacecraft practically stayed within the plasmasphere for the entire orbit.

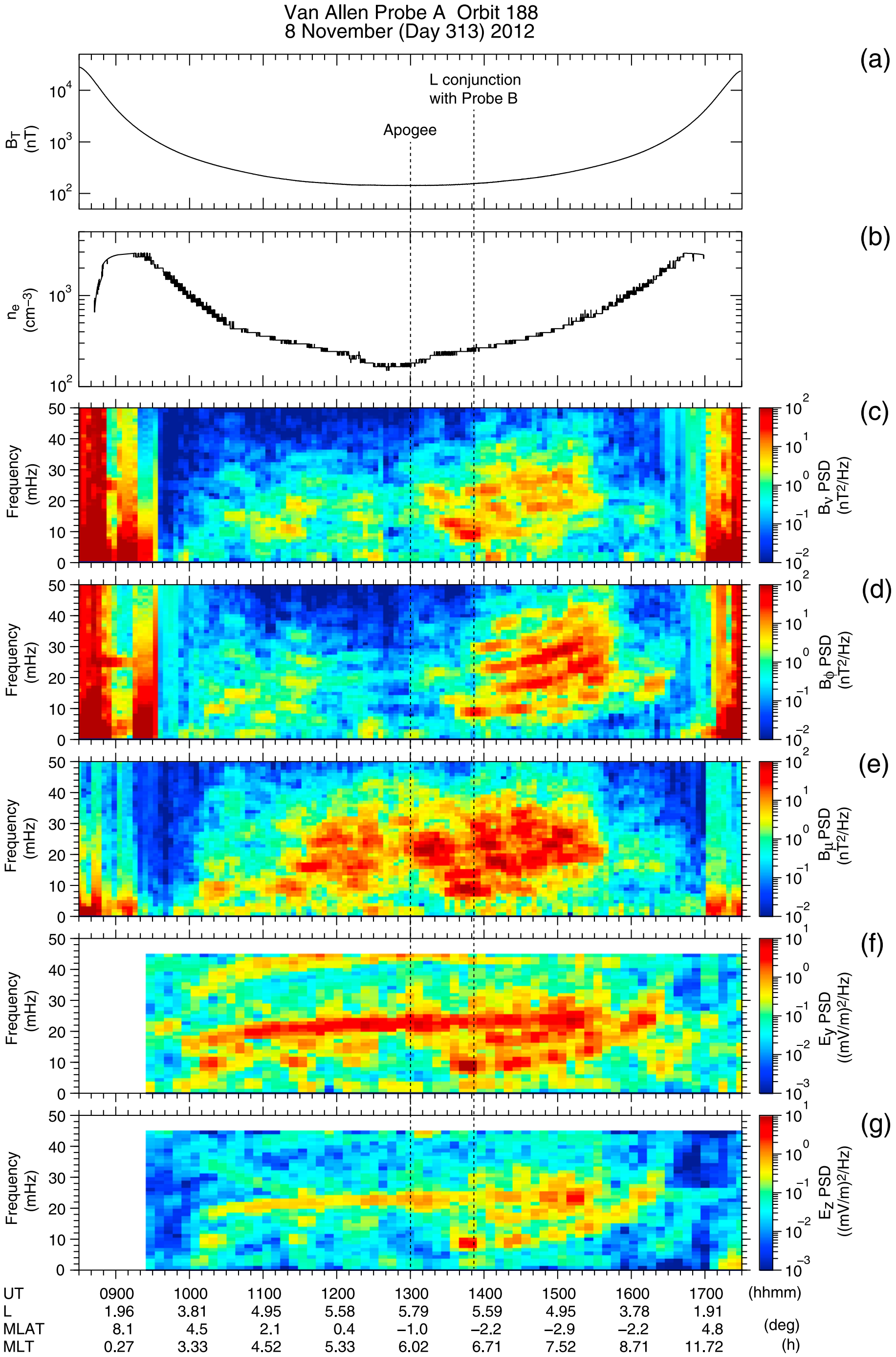

Figure 3. Overview of ULF waves observed by Van Allen Probe A on the orbit shown in Figure 1. The spacecraft position is given at the bottom. The vertical lines indicate the time of apogee (1300 UT) and the time of *L* conjunction with Van Allen Probe B (1351 UT). (a) Magnetic field magnitude. (b) Electron number density estimated from plasma wave spectra. (c–e) Power spectral density (PSD) of the three components of the magnetic field in the MFA coordinates. (f, g) PSD of the two spin-plane components of the electric field in the MGSE coordinates.

The magnetic field dynamic spectra (Figures 3c–3e) show oscillations from 1000 UT to 1630 UT, between 5 and 40 mHz, and in both the compressional (B_μ) and transverse (B_ν and B_ϕ) components. The spectral intensity of the oscillations is high compared with those observed on other Van Allen Probe orbits in the same local time sector. However, the maximum root-mean-square (RMS) amplitude of the oscillations during the selected event is only ~1 nT (shown in Figure 6h), which is a small fraction of the background magnetic field intensity (>100 nT). The B_μ spectral power is strongest between 1300 UT and 1530 UT, when the spacecraft was in the prenoon sector, suggesting a dayside energy source for the ULF waves. Peak B_μ power occurs at multiple frequencies at a given time, but the frequencies do not vary with L in a very systematic way. The B_ϕ component also exhibits spectral enhancements in the same frequency band but with regularly spaced spectral peaks that rise in frequency as the spacecraft L decreases. Similar B_ϕ spectral features have been reported at other elliptically orbiting equatorial satellites [*Engebretson et al.*, 1986; *Takahashi et al.*, 2004] and attributed to multiharmonic toroidal standing Alfvén waves [*Takahashi and McPherron*, 1982; *Denton et al.*, 2004]. The B_ν component shows spectral structures intermediate of B_μ and B_ϕ with the lowest intensity overall.

The elevated spectral intensities seen near apogee, before 0930 UT and after 1630 UT, are artifacts that occur as a result of Fourier transforming nongeophysical large-amplitude field changes. The changes include the magnetic field jump associated with magnetometer range switch, spacecraft crossing of the terminator when the attitude information from the Sun sensor is lost, and imperfect detrending of magnetic field variations first by the removal of a model field (see section 2) and then by the removal of the best fit quadratic function (in time) from the measured field. The detrend scheme works well for $L > 2$, but it may leave a large residual at $L < 2$, where the magnetic field has a large magnitude. Also, the larger digitization step (2 nT) of the magnetometer, which is used below $L \sim 2$, elevates the instrumental noise floor and masks low-amplitude ULF oscillations.

The E_y and E_z spectra (Figures 3f and 3g) show two groups of spectral peaks. In one group, the frequencies vary with L similar to what we see in the B_ϕ spectra. This group is attributed to toroidal waves. In another group, which consists of a strong peak at ~22 mHz and a weak peak at its second harmonic ~44 mHz, the frequencies vary only slightly with UT or L. The spectral peaks in this latter group (referred to as noise lines) center on the 1/4 and 1/2 spacecraft spin frequency of 92 mHz.

From an examination of the Van Allen Probe A data for orbits 180 through 200, we find the following features of the noise at ~22 mHz:

1. The noise is present on all orbits.
2. On each orbit, the frequency of the noise rises from ~20 mHz at the beginning to ~25 mHz at the ending, with frequency reset occurring around the perigee.
3. The full width at half maximum (FWHM) bandwidth of the noise line is smaller than 5 mHz.
4. The amplitude of the noise varies significantly from orbit to orbit and also during an orbit.
5. The amplitude is lower than 0.4 mV/m in the E_y component and lower than 0.1 mV/m in the E_z component.

These features lead us to conclude that the noise lines are of a nongeophysical origin. Although the origin has not been identified, it is usually easy to distinguish the noise lines from naturally occurring spectral peaks by examining dynamic spectra.

3.2. Multiharmonic Toroidal Waves

To better characterize the toroidal waves, we have determined the frequencies of the spectral peaks of the B_ϕ and E_y components using the following procedure. First, we compute the power spectral density (PSD) of each field component by applying the Fourier transform to data in a 15 min window that is moved forward in 5 min steps, smooth the PSD by taking three-point averages in the frequency domain, and identify all spectral peaks. Second, for each spectral peak, we determine the FWHM, which is specified by the lower limit f_0 and the upper limit f_1. Third, following *Takahashi and McPherron* [1982], we compute the weighted frequency f_{pw} of the spectral peak given by

$$f_{\text{pw}} = \frac{\int_{f_0}^{f_1} \text{PSD}(f) f df}{\int_{f_0}^{f_1} \text{PSD}(f) df}, \tag{1}$$

where the actual integration is done by taking the sum of the discrete Fourier components between f_0 and f_1.

Once a complete list of the weighed frequencies is obtained for the selected orbit, we plot the frequencies versus UT and use an interactive method similar to that described by *Takahashi et al.* [2010b] to assign harmonic numbers to those peaks that form a well-defined harmonic structure. Here the harmonic number

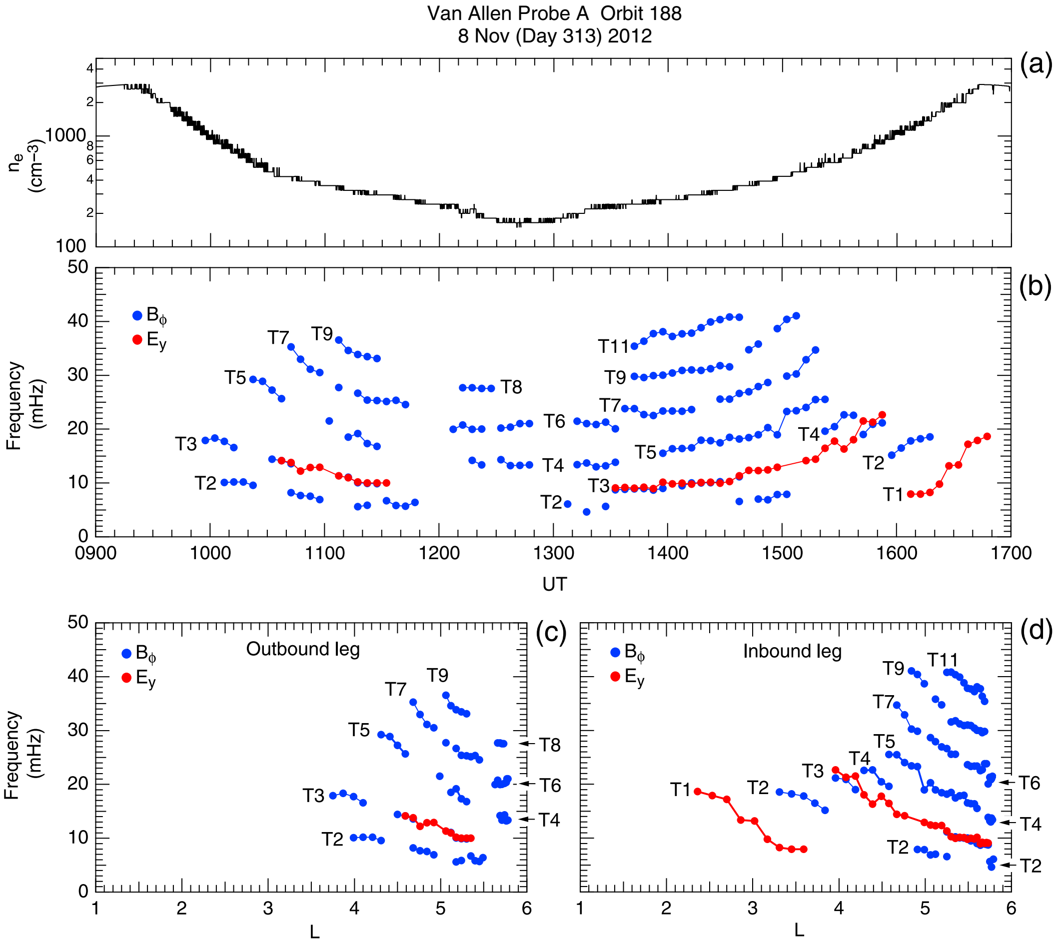

Figure 4. Observed or derived parameters at Van Allen Probe A on the orbit shown in Figure 1. (a) Electron density. (b) Frequencies of multiharmonic toroidal waves determined by spectral analysis of the B_ϕ (blue dots) and $E_{y\mathrm{MGSE}}$ (red dots) components. Toroidal wave harmonic numbers are assigned to the frequencies. (c, d) Toroidal wave frequencies versus L, plotted separately for the outbound and inbound legs.

refers to the standing Alfvén wave mode structure along the background magnetic field. For standing waves with both ionospheric foot points fixed, which is the assumption we make, the lowest-order mode has half a wavelength between the foot points [*Sugiura and Wilson*, 1964]. This mode is called the fundamental mode, and we assign harmonic number 1 to it. The second harmonic (mode number = 2) has a full wavelength between the foot points. The mode numbers for the third and higher harmonics are defined accordingly.

In determining the harmonic mode for the observed spectral peaks, we rely on the frequency spacing between spectral peaks, the phase relation between the electric and magnetic field perturbations, and the MLAT of the spacecraft relative to the nodes or antinodes of the oscillations in the electric field and magnetic field. Numerical models of the standing waves on dipole field lines [e.g., *Cummings et al.*, 1969] provide quantitative information on the frequencies and nodal structures. Presence of multiple harmonics over time and satellite L shell is very helpful in the mode identification, because it allows us to determine the harmonic modes consistently even when a few harmonics exhibit weak signatures.

Figure 4 shows the weighted peak frequencies, plotted versus UT (Figure 4b) and versus L for the outbound (Figure 4c) and inbound (Figure 4d) legs. The notation Tn is used to label the nth harmonic of toroidal standing Alfvén waves. Peaks are detected from $L = 3.8$ to $L = 5.8$ (apogee) on the outbound leg and from $L = 2.6$ to $L = 5.8$ on the inbound leg. Proximity of the spacecraft to the dayside wave energy source (discussed below) explains why waves penetrate to lower L on the inbound leg. The T1 and T3 modes are detected in E_y, while the T2 to T11 modes are detected in B_ϕ. Overall, the odd harmonics are more prevalent than the even harmonics. The T3 mode is detected in both B_ϕ and E_y at the same or very

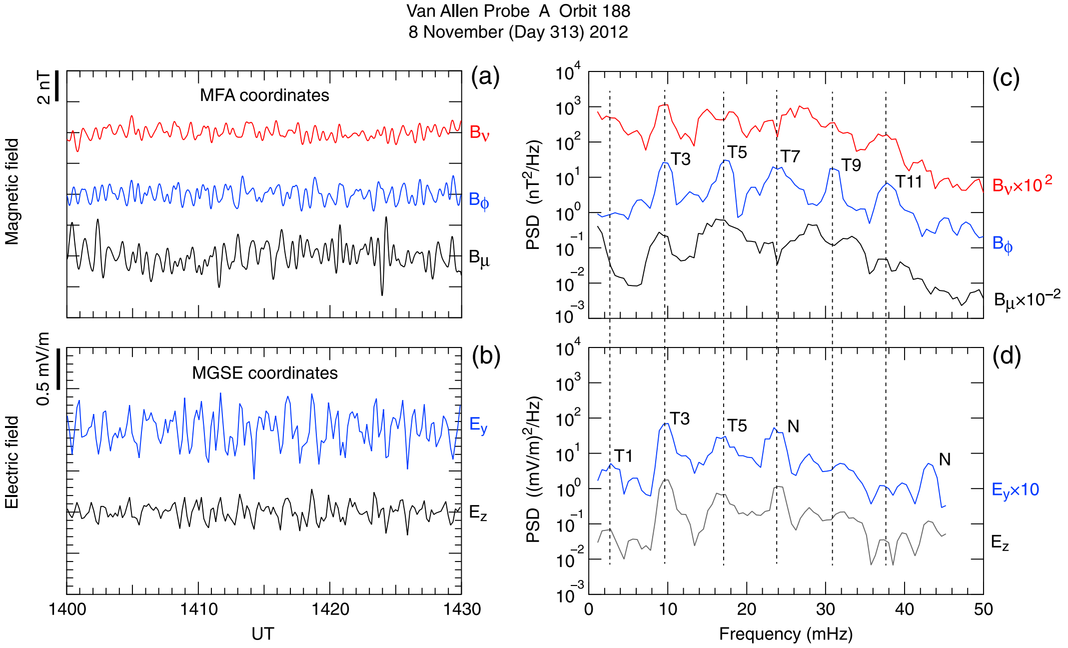

Figure 5. Waveform and PSD of the **B** and **E** fields at Van Allen Probe A during the intense ULF wave activity observed on the orbit shown in Figure 1 at 1400–1430 UT. (a) Magnetic field time series. (b) Electric field time series. (c) Magnetic field power spectra. The power of the B_ν and B_μ components is multiplied by a factor shown on the right. Spectral peaks attributed to multiharmonic toroidal waves are labeled T3 (third harmonic) through T11 (eleventh harmonic), and vertical dashed lines are drawn through these peaks. (d) Electric field power spectra. A weak peak appears at the fundamental mode (T1). The peaks labeled "N" are caused by noise generated at the spacecraft.

similar frequencies, giving us confidence in the mode identification. The monotonic L dependence of the frequencies and the even spacing between them are consistent with previous observations [*Takahashi et al.*, 1990, 2004] and theoretical models [e.g., *Orr and Matthew*, 1971; *Lee and Lysak*, 1989]. The detection of the T2, T4, and T6 peaks (even modes) only in B_ϕ when the spacecraft was very close to the magnetic equator (1200–1300 UT, see Figure 2b) and the detection of only the T1 and T3 peaks (odd modes) in E_y on the entire orbit are also consistent with the standing wave nodal structure predicted by theory.

Figure 5 shows the waveforms and Fourier spectra of all **B** and **E** components at Van Allen Probe A for a 30 min period during the intense ULF wave activity seen in Figure 3. At the center (1415 UT) of the selected time period, the spacecraft was located at $L = 5.5$, MLAT $= -2.4°$, and MLT $= 6.9$ h. In the **B** field time series plots (Figure 5a), B_μ exhibits the largest amplitude (~2 nT peak-to-peak) overall, with a waveform that differs from those of the transverse components. The power spectra of the three **B** field components all show spectral enhancement above ~5 mHz, an overall power maximum at 20–30 mHz, and several peaks (Figure 5c). The spectral peaks of the B_ϕ component are regularly separated by ~7 mHz and are attributed to odd modes T3 through T11. Not all peaks in the B_ν or B_μ spectrum match those of the B_ϕ spectrum.

Figure 5b shows that oscillations appear both in the E_y and E_z components with little phase delay and an amplitude ratio of 1 to ~0.5. This feature can be explained by a finite projection of the E_ν perturbations of the toroidal waves to both the z and y axes of the MGSE coordinates. For a quantitative evaluation of this effect, we examine the relevant coordinate transformation at Van Allen Probe A for the epoch of 1415 UT. In the GSE coordinates, the spacecraft position was (1.29, −4.90, −2.04 R_E), the spin axis direction was (0.947, −0.029, 0.321), and the model magnetic field (very close to the observation) is (−18.5, −87.1, 149.7 nT). From these vectors, we can determine the direction of the axes of the MFA and MGSE coordinates, following the definition given in section 2. We find that the radial direction of the MFA coordinates, $\mathbf{e}_\nu$, is given in the MGSE coordinates as $\mathbf{e}_\nu = (e_{\nu x}, e_{\nu y}, e_{\nu z}) = (0.111, -0.842, -0.528)$. This last expression indicates that a purely radial electric field oscillation in the MFA coordinates produces E_y and E_z oscillations in the MGSE coordinates that are in phase and have an amplitude ratio of 1 to 0.63. This prediction explains the **E** field data in Figure 5b very well, which is evidence that the measured **E** field oscillations resulted from radially polarized oscillations associated with toroidal waves.

The **E** field spectra (Figure 5d) exhibit peaks at the T1, T3, and T5 modes identified in the B_ϕ spectrum. Note that the T1 and T5 spectral peaks do not appear in Figure 4b at 1400–1430 UT, because the peaks are obscured in the spectra computed using a 15 min data window. Absence of even harmonics is not strange because they have an electric field node at the magnetic equator.

4. Solar Wind Condition and Wave Excitation Mechanism

4.1. Excitation of Upstream Waves

It is well established that ions traveling from the bow shock into the incoming solar wind generate ULF waves in the Pc3–Pc4 pulsation band (7–100 mHz) called upstream ULF waves [*Fairfield*, 1969; *Troitskaya et al.,* 1971] and that the waves propagate into the magnetosphere as fast mode waves, subsequently coupling to toroidal standing Alfvén waves at multiple field line harmonics [*Hasegawa et al.*, 1983; *Takahashi et al.*, 1984a, 1984b; *Engebretson et al.*, 1986; *Clausen et al.*, 2009].

Upstream waves are excited to large amplitude in the region upstream of the bow shock surface if the bow shock normal makes a small angle to the interplanetary magnetic field (IMF) (quasi-parallel shock). When a parallel shock is formed at the bow shock nose, a large portion of the bow shock around it becomes quasi-parallel, and as a consequence a large volume of the upstream region is filled with upstream waves. This leads to strong ULF waves in the magnetosphere over a wide range of MLTs. To describe the IMF orientation at the bow shock nose, we use the IMF cone angle, $\theta_{xB} (\equiv \cos^{-1}(|B_{x\mathrm{GSE}}|/B_\mathrm{T}))$, where $B_{x\mathrm{GSE}}$ is the component of IMF along the Sun-Earth line, and B_T is the magnitude of IMF. Statistical analyses indicate that $\theta_{xB} < 50°$ is required for the upstream waves to affect magnetospheric ULF waves, with the strongest waves appearing in the magnetosphere when $\theta_{xB} < 20°$ [e.g., *Greenstadt et al.*, 1980]. The frequency of the upstream waves, f_uw, also depends on the IMF, because excitation of the upstream waves involves cyclotron resonance interaction of the backstreaming ions [*Fairfield*, 1969]. A theoretical model predicts $f_\mathrm{uw}(\mathrm{mHz}) = 7.6B_\mathrm{T}(\mathrm{nT})\cos^2\theta_{xB}$ [*Takahashi et al.*, 1984a], which is close to empirically obtained formulas [*Troitskaya and Bolshakova*, 1988]. Evidence in support of the upstream source mechanisms for magnetospheric ULF waves near the magnetic equator has been reported at geosynchronous orbit [*Takahashi et al.*, 1984a; *Yumoto et al.*, 1984] and beyond [*Engebretson et al.*, 1986]. We demonstrate below that the same mechanism explains our plasmaspheric observations. We also find properties that are unique, including excitation of high-order harmonics and distribution of strong wave energy mainly to the odd harmonics.

Figure 6 shows parameters that provide evidence for the wave excitation mechanism described above. Figure 6a shows the *Dst* index for a 20 day period including the period of interest (the thick horizontal bar). The next six panels show the solar wind velocity V_sw (Figure 6b), the number density N_sw (Figure 6c), the dynamic pressure P_sw ($= m_\mathrm{p}N_\mathrm{sw}V_\mathrm{sw}^2$, where m_p is proton mass, Figure 6d), the IMF magnitude (Figure 6e), the IMF cone angle (Figure 6f), and the upstream wave frequency given by *Takahashi et al.* [1984a] (Figure 6g). The source of these solar wind parameters are the OMNI data with 1 min time resolution, which were based on observations made by the Wind spacecraft 256 R_E sunward of the Earth and time shifted to the bow shock nose (http://omniweb.gsfc.nasa.gov/ow_min.html). Figure 6h shows the RMS amplitude for each of the three components of the magnetic field at Van Allen Probe A that is obtained by taking the square root of the power spectral density integrated over 5–40 mHz. The spectra were computed in a 15 min data window with a 50% overlap in successive steps.

From 0930 to 1630 UT, during which the RMS amplitudes are accounted for by real ULF waves, the B_μ component exhibits the largest amplitude overall (up to 0.9 nT observed at 1400 UT), implying the presence of fast mode waves that are generated by the upstream source mechanism. The IMF cone angle during this period was mostly around 30°, consistent with the upstream source mechanism. However, excursion of the IMF cone angle to values greater than 60° occurred twice, one at ~1220 UT and another at ~1530 UT. A reduction of the B_μ amplitude by a factor of ~2 to 0.3 nT occurred in association with the first cone angle excursion, which can be attributed to reduced upstream wave amplitude. A reduction of the B_μ amplitude is also observed in association with the second cone angle excursion. However, after 1530 UT, the B_μ amplitude did not recover to the previous level although the cone angle became small (~30°) again. We attribute the low amplitude after 1530 UT to the decrease of the spacecraft L value ($L < 4.5$), with the assumption that the amplitude of externally driven fast mode waves decreases with distance from the magnetopause. When the IMF cone angle is small, the predicted upstream wave frequency is in the 10–30 mHz range (Figure 6g), which covers the center of the band occupied by the observed plasmaspheric

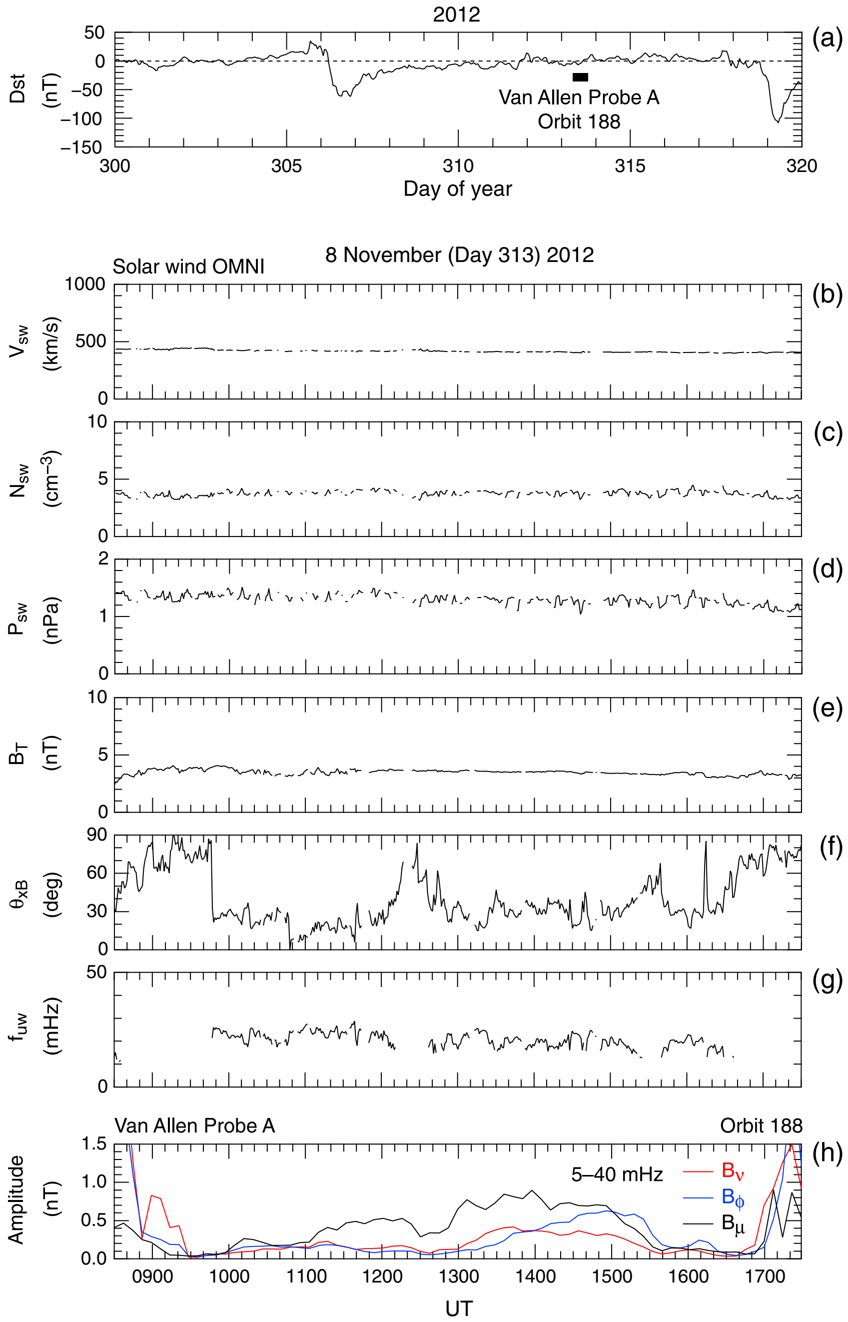

Figure 6. (a) *Dst* index for a 20 day period including 8 November 2012. (b–g) Solar wind parameters for the time period shown in Figure 1. The velocity (V_{sw}), density (N_{sw}), and the magnetic field magnitude (B_T) are 1 min values provided as the time-shifted OMNI data. The dynamic pressure (P_{sw}), IMF cone angle (θ_{xB}), and the predicted upstream wave frequency (f_{uw}) are derived from the OMNI data. (h) Root-mean-square amplitude of the three components of the magnetic field in the 5–40 mHz band. The enhancements seen near the perigee, before 0930 UT and after 1630 UT, are not real.

ULF waves. This is also evidence for the upstream source. The solar wind velocity, density, and the dynamic pressure were all steady, which implies that these parameters played little role in modulating the amplitude of the plasmaspheric ULF waves. However, we should note that given the 1 min resolution of the solar wind OMNI data, we cannot rule out the possibility that there were fluctuations with periods shorter than 1 min that were already present in the solar wind before it reached the foreshock and that these fluctuations propagated into the plasmasphere. The *Dst* value was close to 0 (Figure 6a), which makes internal excitation of Pc3–Pc4 waves unlikely. We conclude that the data shown in Figure 6 strongly support the upstream waves as the source of the plasmaspheric ULF waves observed by the Van Allen Probes.

4.2. Tailward Propagating Fast Mode Waves

Fast mode propagation expected from the upstream source mechanism can be tested by examining the phase and amplitude relationship between the electric field and magnetic field oscillations associated with the mode. The waves will propagate isotropically from the subsolar magnetopause [*Tamao*, 1964], where transmission of upstream waves is expected to be strong when the IMF cone angle is small [e.g., *Greenstadt et al.*, 1980]. When observed away from the subsolar region, the waves should appear predominantly tailward propagating. If fast mode waves propagate tailward (the −*x* direction) perpendicular to the background magnetic field that is directed northward (the *z* direction), they will produce perturbations in the magnetic field *z* component, B_z, and in the electric field *y* (dawn-dusk) component, E_y. The phase delay between the B_z and E_y oscillations will be 180°, corresponding to Poynting flux-directed tailward. Meanwhile, the amplitudes of these components, δB_z and δE_y, are related to the wave phase velocity. In cold plasma, which is a good approximation in the plasmasphere, the fast mode velocity is the same as the Alfvén velocity V_A. Therefore, we have

$$\frac{\delta E_y}{\delta B_z} = V_A. \tag{2}$$

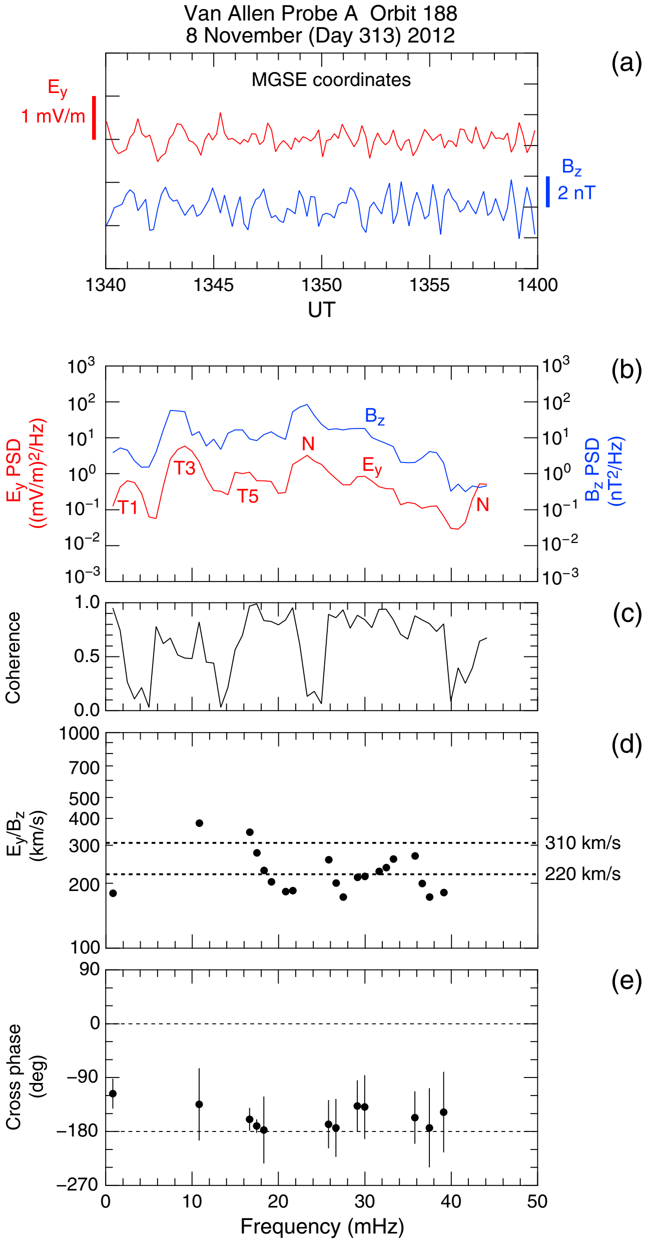

Figure 7. Cross-spectral analysis of the E_y and B_z components at Van Allen Probe A. (a) Time series plots of the field components. (b) PSD. (c) Coherence. (d) E_y to B_z amplitude ratio, shown if coherence is higher than 0.8. (d) Cross phase, shown if coherence is higher than 0.8. The error bars give 95% confidence intervals.

Figure 7 demonstrates that the observed waves indeed have the properties of fast mode waves. The data shown are from Van Allen Probe A covering a 20 min period near the apogee. Here we use ~11 s **B** and **E** vector samples defined in the MGSE coordinates, which are appropriate for the wave propagation geometry assumed above. The E_y to B_z amplitude ratio (Figure 7d) and the cross phase (Figure 7e) are shown when the coherence (Figure 7c) is higher than 0.8. The amplitude ratio is the ratio of the square root of the E_y PSD to the square root of the B_z PSD. In the time series plots (Figure 7a), the expected antiphase oscillations are visible, for example, from 1340 to 1344 UT. The shape of the power spectra (Figure 7b) is similar between the two field components (the E_y spectral peaks at 22 mHz and 44 mHz, labeled "N" for noise, are artifacts). The amplitude ratio, which has the dimension of velocity, is close to the 310 km/s that is obtained from the phase delay analysis of B_μ oscillations and to the local Alfvén velocity of 210 km/s that is obtained from the measured magnetic field magnitude and the mass density that is estimated from the measured electron density, assuming that all ions are protons (see section 6.2). Finally, the cross phase is close to $-180°$. We conclude that both the amplitude ratio and cross phase are consistent with tailward propagating broadband fast mode waves.

We note that the E_y oscillations result from both tailward propagating fast mode waves and toroidal waves. This can be seen in Figures 5c and 5d, where peaks in E_y sometimes match those of B_ϕ, and sometimes those of B_μ, for example, at 28 mHz. The contribution from the toroidal wave component is probably the reason for the low coherence observed at some frequencies, for example, around the E_y spectral peaks associated with the T1, T3, and T5 modes. Toroidal waves extract energy from the driver fast mode waves. However, once the toroidal waves have gained energy, they start to oscillate at their own eigenmode frequencies, thereby losing coherence with the driver waves. This explanation would be particularly valid when the driver waves are not steady.

Fast mode waves originating from the upstream waves might excite plasmaspheric cavity resonance (or virtual resonance) [*Allan et al.*, 1986; *Lee*, 1998] in addition to toroidal waves. However, it is not clear whether the cavity mode was excited in the present event. Unlike in the previous studies that reported a single outstanding spectral peak at ~15 mHz [*Takahashi et al.*, 2009] or ~11 mHz [*Takahashi et al.*, 2010a] as evidence of the mode, the spectrum of the B_μ component in our event (Figures 3e and 5c) exhibits multiple peaks and their frequency and intensity change with time. Investigating this further would require comparing the Van Allen Probes data with data from other sources, e.g., ground magnetometers and the GOES geostationary satellites. Such a study is beyond the scope of this paper.

4.3. North-South Symmetry and Frequency Range of Source Waves

It is interesting that prominent peaks in the B_ϕ spectrum occur only at odd harmonics (Figure 5c) although the spacecraft was very close to the magnetic equator (|MLAT| = 2.2–2.6°). The magnetic equator is the location of B_ϕ nodes of odd-mode standing Alfvén waves and the location of B_ϕ antinodes of even-mode waves [*Sugiura and Wilson*, 1964; *Denton et al.*, 2004]. Therefore, we would expect the B_ϕ component to exhibit strong signatures of even harmonics and weak signatures of odd harmonics, when observed near the equator. Here we assume that broadband fast mode waves couple to toroidal waves at multiple harmonics. To explain the dominance of odd-mode waves, we must note that not only the frequency range but also the spatial structure of the external disturbances control which harmonics are excited. The dominance of the odd harmonics can be explained by external disturbances that are symmetric about the magnetic equator, which will deliver little power to the even-mode waves.

This consideration on the wave symmetry led us to examine the IMF orientation with respect to the magnetic (dipole) equator. During 1400–1430 UT, which is the period covered by Figures 5c and 5d, the IMF made an average angle of +22° from the equator with a standard deviation of 6°, according to the OMNI data. The solar wind velocity vector made an average angle of +9° from the equator with a standard deviation of 0.5°. These vector orientations imply that the parallel shock was formed slightly south (−10° to −20°) of the dipole equator and the upstream waves had the largest amplitude there. This configuration would be favorable for exciting the T1 and T3 modes, which have an antinode of azimuthal field line displacement (ξ_ϕ) at the equator.

To make this argument more quantitative, we show in Figure 8 the MLAT dependence of the amplitude of ξ_ϕ (Figure 8a), B_ϕ (Figure 8b), and E_ν (Figure 8c) of the T1–T3 modes obtained by solving the toroidal wave equation of *Cummings et al.* [1969]. The calculation is done for $L = 5.5$ using the $\alpha = 0$ mass density model (see equation (5)). In the ξ_ϕ plot, we note that at the location of Van Allen Probe A (MLAT = −2.4°), the T1 and T3 modes have amplitudes close to the respective equatorial peak values. The T2 mode has a ξ_ϕ antinode at about MLAT = −15°, around the expected center of action of the external waves. Therefore, not only the T1 and T3 but also the T2 modes could be excited by the upstream waves.

E_ν (Figure 8c) has the same symmetry about the magnetic equator as ξ_ϕ, having an antinode (node) of odd (even) harmonics located at the equator. This explains why the T3 mode is clearly seen in the E_y spectra, and the same can be said of the T5 mode (not shown in Figure 8). Similarly, the T1 mode should be very easy

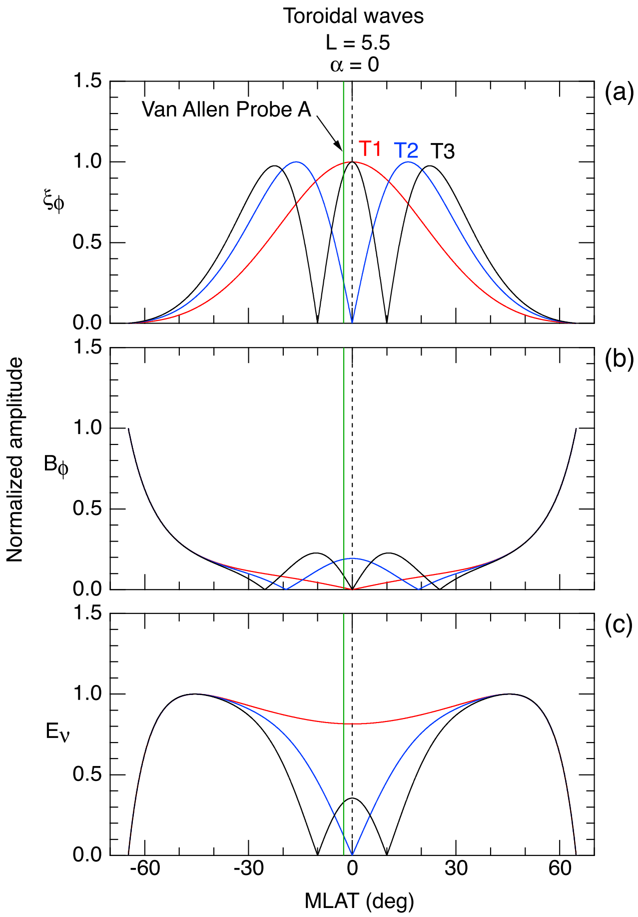

Figure 8. MLAT dependence of the theoretical amplitude of the fundamental (T1), second (T2), and third (T3) harmonics of toroidal waves at $L = 5.5$. The mass density variation along the field line is specified by $\alpha = 0$ (see equation (5)). The vertical green line indicates the location of Van Allen Probe A at 1415 UT. The amplitude is normalized to the peak value. (a) Azimuthal field line displacement. (b) Azimuthal component of the magnetic field. (c) Radial component of the electric field.

to detect. However, Figure 5d shows that the PSD at the T1 mode (~3 mHz) is 14 times lower than that at the T3 mode (~10 mHz). Clearly, the energy delivered to the T1 mode was very low. A possible interpretation of this feature is that the source waves in the upstream region had little energy below 5 mHz. This will certainly be the case if the upstream waves are the main energy source.

B_ϕ (Figure 8b) has a symmetry opposite to that of ξ_ϕ and E_ν, with a node (antinode) of odd (even) harmonics located at the equator. In general, when a spacecraft is very close to the equator, it will be easy to detect the B_ϕ signatures of the even harmonics, but not the odd harmonics [*Takahashi and McPherron*, 1982]. On the contrary, the odd harmonicsdominate the B_ϕ spectra shown in the present study. This unique spectral feature can be explained only by strong excitation of the odd harmonics and nearly complete absence of the even harmonics. It is not clear whether the location of the quasi parallel shock alone can explain this disparity between odd and even harmonics. The foreshock geometry discussed above "certainly" has a certain degree of north-south asymmetry, which makes it difficult to explain the observed higher-order odd harmonics up to the eleventh.

A possible additional reason for the dominance of the odd-mode waves is the way fast mode waves propagate in the magnetosphere. *Lee* [1996] theoretically showed that, as externally driven fast mode waves propagate to lower *L*, their energy is narrowly confined to the equatorial region due to the variation of the Alfvén speed along the magnetic field line. Observations in support of this effect can be seen in the AMPTE/CCE magnetic field statistical study presented by *Takahashi and Anderson* [1992]. The equatorial fast mode waves will couple only to odd-mode standing Alfvén waves.

It is also possible that external fast mode waves experience cutoff (reflection) within the magnetosphere [*Tamao*, 1978; *Lee*, 1996] and cannot reach the plasmasphere below 5 mHz, which explains the weak appearance of the T1 mode noted above. This occurs in the presence of an inward gradient of fast mode velocity, which is expected throughout the magnetosphere except at the plasmapause or plasma plume density gradient. Previous electric field observations indicated that strong Pc5 power exists at geostationary orbit [*Junginger et al.*, 1984] but not in the plasmasphere [*Hartinger et al.*, 2010], in support of this mechanism.

5. Two-Spacecraft Phase Delay Analysis

In this section, we examine wave propagation speed and the radial structure of field line resonance by applying phase delay analysis to data from the Van Allen Probes. Phase delay analysis has been used to

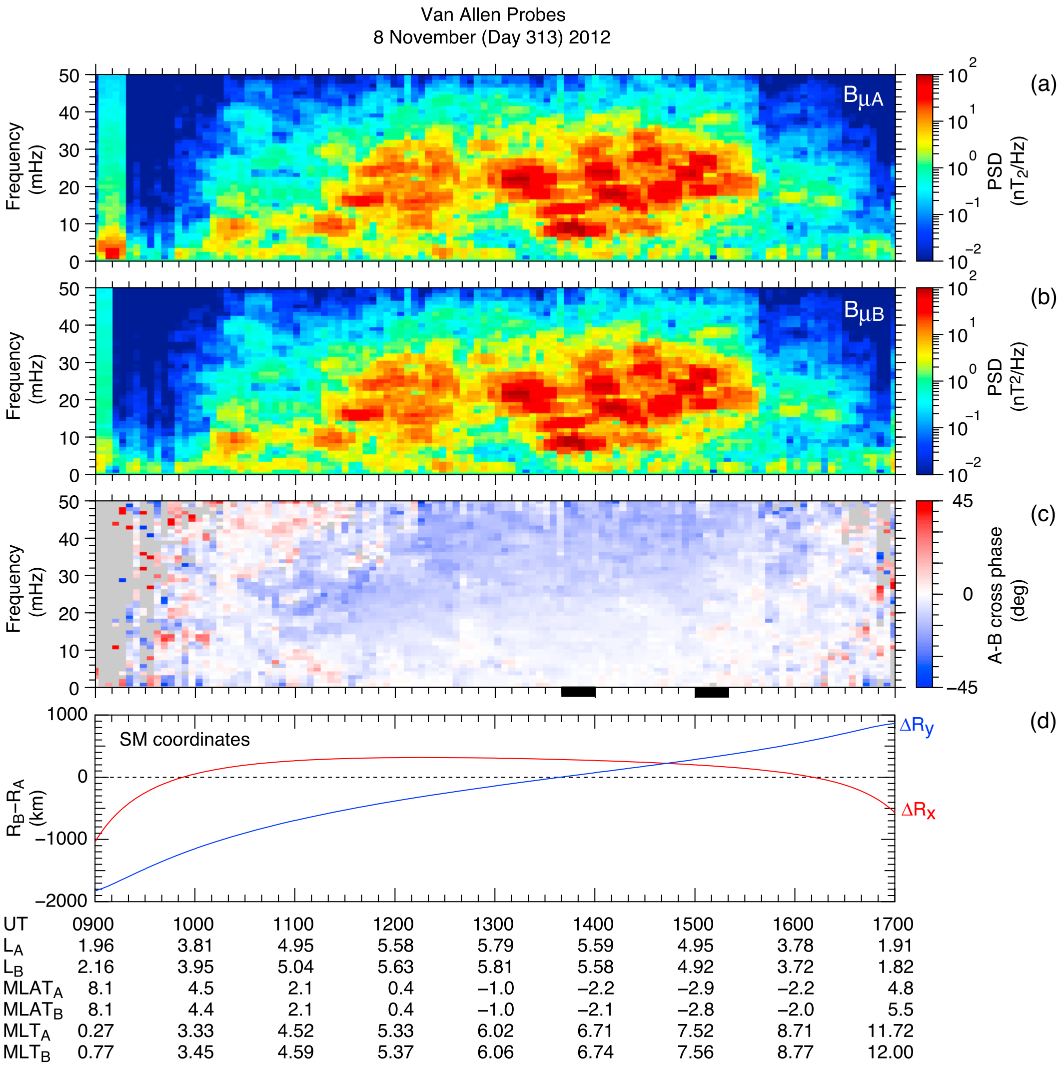

Figure 9. (a, b) Dynamic power spectra of the B_μ components from Van Allen Probes A and B, labeled $B_{\mu A}$ and $B_{\mu B}$, respectively. (c) Dynamic $B_{\mu A}$-$B_{\mu B}$ cross-phase spectra, where the phase is defined positive for phase propagation from Van Allen Probe A to Van Allen Probe B. The cross phase is shown with the color key on the right only when the $B_{\mu A}$-$B_{\mu B}$ coherence (not shown) is higher than 0.7. Pixels are shown in gray if the coherence is lower. The thick horizontal bars along the time axis indicate time periods selected for detailed analysis shown in Figure 10. (d) Spacecraft separation (B minus A) along the *x* and *y* axes of the SM coordinates.

estimate the azimuthal wave number of ULF waves observed by geostationary satellites [*Takahashi et al.*, 1984b, 1985], Cluster [*Eriksson et al.*, 2006], and THEMIS [*Sarris et al.*, 2009, 2013]. However, in these studies, observations were made mostly outside the plasmasphere, and the phase variation arising from the radial structure of field line resonance was not fully considered. In section 5.1, we will examine the phase delay of compressional (B_μ) oscillations. The oscillations are not expected to have the strong *L* shell variations that the transverse modes should exhibit and are therefore easier to analyze and to introduce the cross-phase observations and analysis. Then in sections 5.2–5.4, we will examine the phase delay of transverse (B_ϕ) oscillations. The oscillations are more complex to analyze and will require a more careful consideration of the relative spatial locations of the two Van Allen Probe spacecraft during the analysis intervals.

5.1. Phase Delay of B_μ Oscillations

Figure 9 displays the power spectra (Figures 9a and 9b) and cross-phase spectra (Figure 9c) computed from the B_μ components measured at the two spacecraft. In addition, the spacecraft separation along the *x* and *y* axes of the SM coordinates, denoted ΔR_x and ΔR_y, is shown (Figure 9d).

In the color display of the B_μ cross phase (Figure 9c), we see a smooth transition of the phase with both time and frequency but not any pattern that resembles the fine spectral structures seen in the dynamic spectra (Figures 9a and 9b). Before ~1100 UT and after ~1600 UT, the cross-phase pattern is noisy, which can be explained by the low B_μ power level at both spacecraft. Between ~1200 UT and ~1600 UT, the cross phase is near zero (white) at low frequency and negative (blue) at high frequency. In our calculation of the cross phase, its sign is defined to be positive for signal propagation from Van Allen Probe A to Van Allen Probe B (there is no $2n\pi$ ambiguity, because the spacecraft separation was small). Therefore, if $\Delta R_x > 0$, negative cross phase means tailward propagation of oscillations. The possibility that the cross phase results from a large wave normal component along the y (dawn-dusk) direction can be dismissed, because the cross phase does not switch sign when ΔR_y changes from negative to positive (1340 UT). To characterize the phase delay more quantitatively, we next examine the phase delay at 1340–1400 UT and 1500–1520 UT, which are chosen to represent different spacecraft separations. These periods are marked by the thick horizontal bars at the bottom of Figure 9c.

The time series and corresponding spectral parameters for the two selected periods are shown in the two columns of Figure 10. In each column, the panels show (from top to bottom), the spacecraft relative distance, time series plots of B_μ for the whole 20 min, the expanded view of a 5 min segment, and the PSD and cross phase computed from the 20 min segment. The cross phase is shown only if the coherence (not shown) is higher than 0.8, with the vertical bars indicating the 95% confidence intervals described by *Green* [1976].

We assume a simple plane wave model in interpreting the measured phase delay of B_μ. For a plane wave having a wave vector $\mathbf{k}$, the phase delay θ measured at two locations separated by $\Delta\mathbf{R}$ is given by $\theta = \mathbf{k}\cdot\Delta\mathbf{R}$. Using the wave phase velocity $V_{\rm ph}$ given by $V_{\rm ph} = \omega/k$, where ω is the angular wave frequency, and the angle δ_k between $\mathbf{k}$ and $\Delta\mathbf{R}$, this equation can be rewritten as

$$V_{\rm ph} = (\omega/\theta)|\Delta\mathbf{R}|\cos\delta_k. \quad (3)$$

With two-spacecraft measurements, it is impossible to determine the direction of $\mathbf{k}$. Therefore, we need to make an assumption on the direction in estimating the wave phase velocity.

During the first 20 min period (Figures 10a–10e), the spacecraft had larger separation along the SM x axis ($|\Delta R_x| \sim 280$ km) than along the y axis ($|\Delta R_y| \sim 40$ km) (Figure 10a). Both the time series (Figures 10b and 10c) and spectra (Figure 10d) are hard to distinguish between the two spacecraft. However, the cross-phase spectrum (Figure 10e) indicates clear phase delay. The cross phase (θ) is negative, and its magnitude increases approximately linearly with frequency (f). A linear f-θ relationship with $\theta = 0$ occurring at $f = 0$ is equivalent to identical waveforms that are time shifted from one location to another, resulting from a wave phase velocity that does not depend on frequency. To determine the phase velocity, we fitted a straight line to the data points in Figure 10e, forcing the line to pass the origin. The slope of the line is equivalent to a time delay (Δt) of −0.89 s, where the minus sign indicates that Van Allen Probe A sees oscillations that are delayed relative to Van Allen Probe B. The phase velocity along the x axis, V_x, is given by $V_x = \Delta R_x/\Delta t$, which is −310 km/s. V_x would be equal to $V_{\rm ph}$ if the waves were propagating along the spacecraft separation vector, corresponding to $\delta_k = 0$ in equation (3).

A simple scenario for the detected phase delay is that the compressional magnetic field oscillations are associated with fast mode waves propagating away from the subsolar magnetopause as described in section 4.2 and reported in the outer magnetosphere [e.g., *Takahashi et al.*, 1994]. We can test this scenario by estimating the fast mode velocity at the spacecraft. In the plasmasphere, the Alfvén velocity $V_{\rm A}(= B(\mu_0\rho)^{-1/2})$ is a good approximation to the fast mode velocity because the plasma β is low. The average magnetic field magnitude and electron number density for 1340–1400 UT are 155 nT and 254 cm^{-3} (evaluated at Van Allen Probe A), respectively, which give $V_{\rm A} = 210$ km/s if we assume that H$^+$ is the dominant ion species. This value of $V_{\rm A}$ is close to the value of V_x (= 310 km/s) derived from the phase delay analysis on the order of magnitude basis, which gives us confidence in attributing the phase delay to fast mode propagation.

The phase delay analysis for the second 20 min period is shown in Figures 10f–10j. In this period, the spacecraft separation had a large y component: $|\Delta R_x| \sim 180$ km and $|\Delta R_y| \sim 320$ km (Figure 10f). However, the time series (Figures 10g and 10h), power spectra (Figure 10i), and cross phase (Figure 10j) are similar

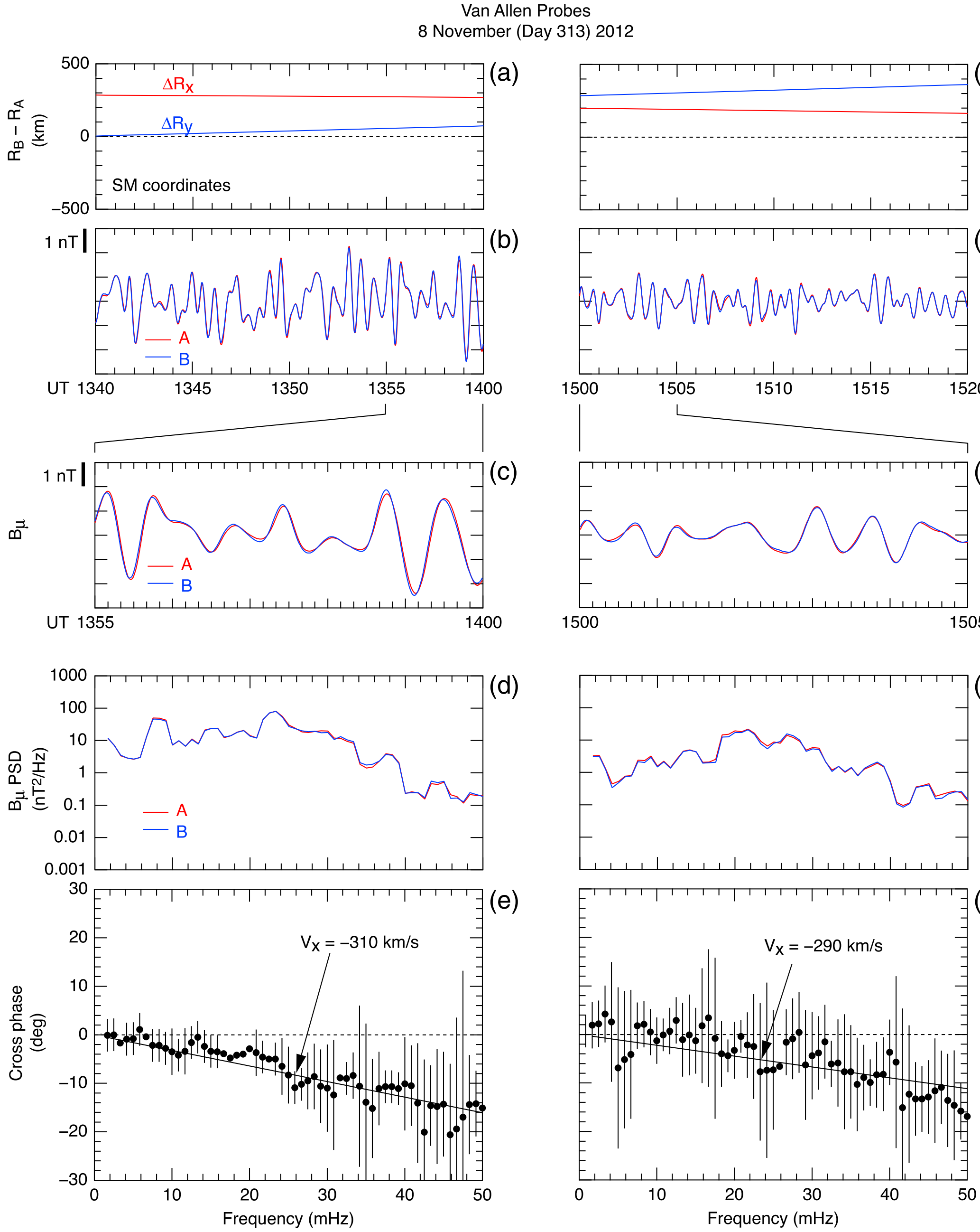

Figure 10. Comparison of B_μ oscillations observed from Van Allen Probes A and B. The two 20 min segments differ in the radial separation of the spacecraft. (a, f) Separation of the spacecraft along the *x* and *y* axes of the SM coordinates. (b, g) Detrended B_μ components from Van Allen Probes A (red) and B (blue). (c, h) Time expanded plots of the B_μ components. (d, i) PSD of the B_μ components. The 20 min segments are used. (e, j) Cross phase between the B_μ components from the two spacecraft. The cross phase and the 95% confidence interval are plotted only when the coherence (not shown) is higher than 0.8. A straight line is fitted to the data points and the corresponding phase velocity V_x is shown.

to those of the first period. The larger error bars in Figure 10j than in Figure 10e, seen at frequencies below ~20 mHz, are attributed to the lower power (and thus lower coherence) in the second period. From line fitting to the cross phase, we get a time delay (Δt) of −0.62 s, which gives $V_x = \Delta R_x / \Delta t = -290$ km/s. Meanwhile, the magnetic field magnitude and electron number density averaged over 1500–1520 UT are 262 nT and 484 cm^{-3}, respectively. From these, we get a fast mode velocity of 260 km/s, which is in good agreement with the velocity obtained from the phase delay analysis.

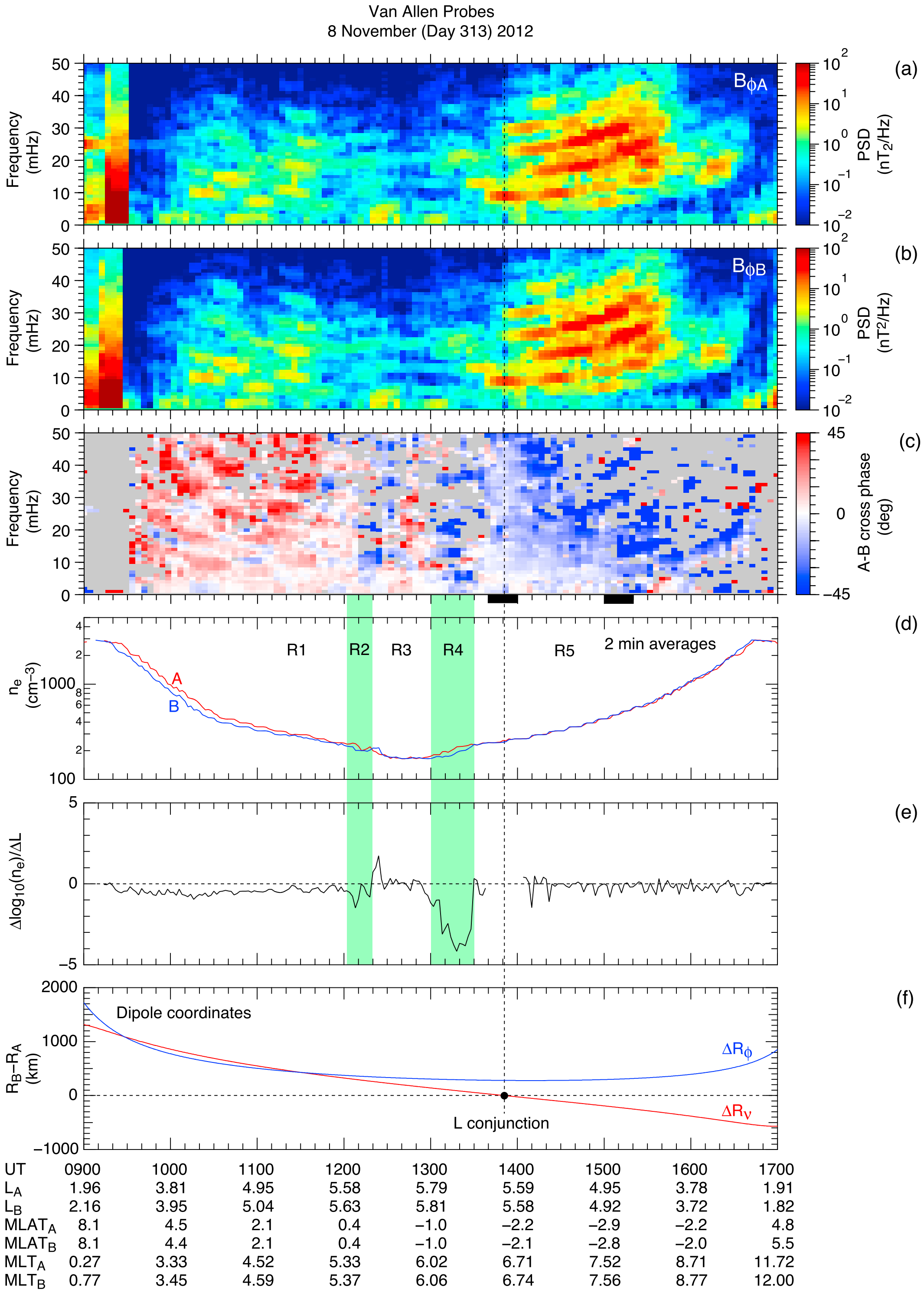

Figure 11. (a, b) Dynamic power spectra of the B_ϕ components from Van Allen Probes A and B, labeled $B_{\phi A}$ and $B_{\phi B}$, respectively. (c) Dynamic $B_{\phi A}$-$B_{\phi B}$ cross-phase spectra. The thick horizontal bars along the bottom time axis indicate periods selected for detailed cross-phase analysis. (d) Two-minute averages of the electron density at Van Allen Probes A (red) and B (blue). (e) *L* gradient of the electron density. See text for its definition. (f) Radial (red) and azimuthal (blue) separation of the spacecraft.

The ~40% difference between the two velocity values, 210 km/s versus 310 km/s, found in the first 20 min period warrants some discussion. We can think of two possible reasons for the difference. First, the larger V_x value is possibly the result of waves propagating not strictly along the spacecraft separation vector. For example, if we assume that the waves were propagating oblique to the separation vector with $\delta_k = 47°$, we obtain a phase velocity of 210 km/s from equation (3), which equals the local fast mode velocity.

Second, the difference could be explained if the propagation speed of large-scale fast mode waves in the inhomogeneous magnetosphere differs from the fast mode speed defined using the local magnetic field and plasma mass density. The observed waves apparently have a parallel wavelength comparable to the field line length itself. Therefore, the observed waves may be propagating at a velocity that is a spatial average along the field line. Because the fast mode velocity in the plasmasphere is usually the lowest at the magnetic equator and increases with MLAT due to the increase of the magnitude of the dipole field, it is possible that the observed waves had a phase velocity that is larger than the locally defined Alfvén velocity very close to the magnetic equator.

5.2. Phase Delay of B_ϕ Oscillations

Figure 11 shows the dynamic power (Figures 11a and 11b) and cross-phase (Figure 11c) spectra of the B_ϕ components. We also include electron density from both spacecraft (Figure 11d). The spacecraft separation vector (Figure 11f) is given in dipole coordinates because they organize the B_ϕ phase structure better than the SM coordinates. The radial and azimuthal components of the separation vector are given by $\Delta R_\nu = R_E \Delta L$ and $\Delta R_\phi = R_E \bar{L} \Delta\phi_{SM}$, respectively, where $\bar{L}$ is the average L value between the two spacecraft.

The cross-spectral properties of B_ϕ differ from those of B_μ in several significant ways. First, the overall coherence is lower for B_ϕ as indicated by many gray pixels in Figure 11c. This means that the coherence length is shorter for B_ϕ than B_μ. Second, the cross phase shows a band structure, which is related to the multiharmonic toroidal waves seen in Figures 11a and 11b. Third, the cross phase is predominantly positive (red) when $\Delta R_\nu > 0$ and negative (blue) when $\Delta R_\nu < 0$, although the cross-phase pattern changes rapidly around the apogee (1210–1330 UT). This last feature is associated with changes in the electron number density shown in Figure 11d and its L gradient $(= (\log_{10} n_{eB} - \log_{10} n_{eA})/(L_B - L_A))$ shown in Figure 11e.

Figure 12 shows the results of B_ϕ phase delay analysis for the same two 20 min periods as in Figure 10 (marked again by the two black bars at the bottom of Figure 11c). During the first 20 min period (Figures 12a–12e), the waveforms are nearly identical between the two spacecraft with only a small time delay (Figures 12b and 12c), which results in very similar power spectra (Figure 12d). The f-θ relationship (Figure 12e) is similar to that of the B_μ component shown in Figure 10e (note the different vertical scales between the figures). The straight line labeled "$V_x = -310$ km/s," which is copied from Figure 10e, strengthens this point.

The second 20 min period (Figures 12f–12j) differs significantly. In the waveform plots (Figures 12g and 12h), we find clear differences between the two spacecraft. Figure 12h shows that the peaks in the red curve (Van Allen Probe A) lag behind those in the blue curve (Van Allen Probe B), which means that phase propagates from lower L to higher L. When mapped to the ionosphere and ground along the magnetic field lines, this would produce poleward phase propagation, a feature previously reported on Pc5 waves observed by ionospheric radar [e.g., *Walker et al.*, 1979]. The power spectra (Figure 12i) still exhibit spectral peaks that match between the two spacecraft, but the coherence (not shown) is degraded at most frequencies. The cross phase has large negative values in the T2 and T3 bands (Figure 12j) compared with the first 20 min period (Figure 12e). Cross phase for $f > 17$ mHz is negative but is highly scattered. In Figure 12j, we have included the straight line ($V_x = -290$ km/s) copied from Figure 10j to emphasize the difference between B_μ and B_ϕ. Obviously, the phase delay of the B_ϕ component strongly depends on the spacecraft radial separation, and we attribute this feature to the radial structure of field line resonance.

5.3. Field Line Resonance Effects on B_ϕ Cross Phase

Figure 13 illustrates the expected cross-phase signatures associated with the radial (L) structure of field line resonance. Figures 13a–13t correspond to the five regions along the orbits of the Van Allen Probes that are marked in Figure 11d as R1 through R5. Figures 13a, 13e, 13i, 13m, and 13q show a schematic L profile of the mass density at the magnetic equator, ρ_{eq}, which is assumed to be time stationary and includes a small dip. The solid portion of the ρ_{eq} curve is based on the electron density measured by the Van Allen Probes. The dashed portion is a possible structure beyond the apogees of the spacecraft that is included for

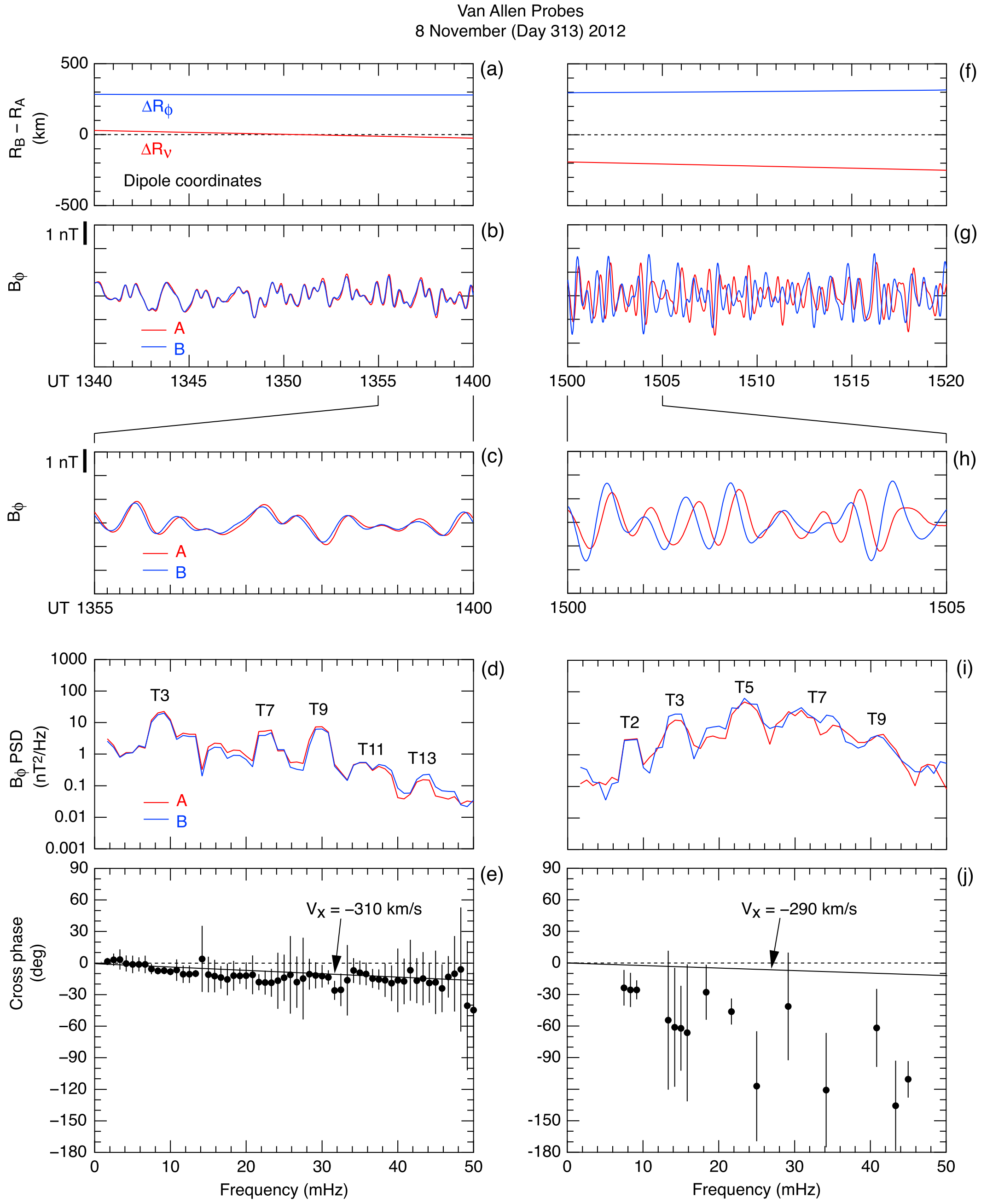

Figure 12. Same as Figure 10 except for the B_ϕ components. Toroidal wave harmonic numbers are assigned to prominent spectral peaks.

illustrative purpose. The locations of the spacecraft are shown by vertical lines. Note that Van Allen Probe A (red line) was at lower *L* than Van Allen Probe B (blue line) from region R1 to region R4, with a position switch occurring between region R4 and region R5. Figures 13b, 13f, 13j, 13n, and 13r illustrate the *L* profile of the frequency of an arbitrary toroidal wave harmonic, f_T, corresponding to the ρ_{eq} profile shown in Figures 13a, 13e, 13i, 13m, and 13q. Figures 13c, 13g, 13k, 13o, and 13s and Figures 13d, 13h, 13l, 13p, and 13t illustrate the power spectra and cross phase of the B_ϕ components, respectively, at the two spacecraft that are expected for field line resonances [*Waters et al.*, 1991].

The cross-phase signature shown in Figures 13d, 13h, 13l, 13p, and 13t is the basis of a successful technique to determine the local toroidal wave frequencies using a pair of ground magnetometers placed with a small latitudinal separation [*Waters et al.*, 1991, 2006]. Here the assumption is that each *L* shell oscillates at its

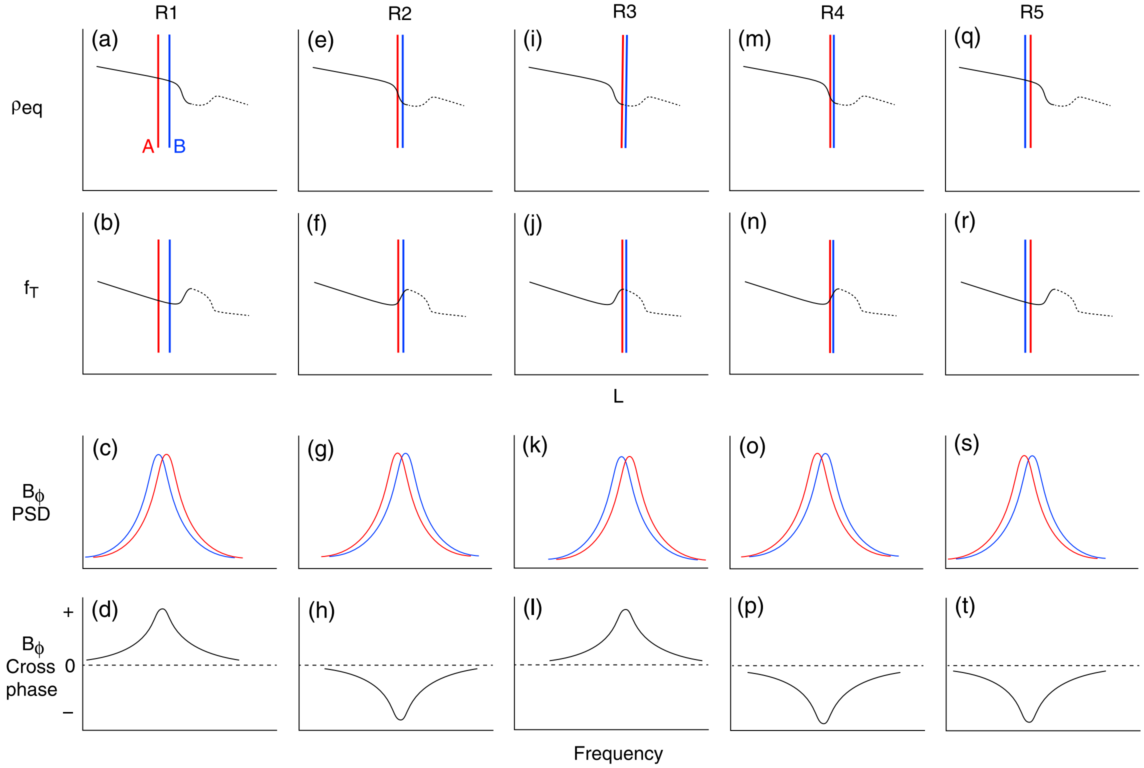

Figure 13. Schematic illustration of two-spacecraft measurements of field line resonance effects. (a–t) The five regions marked in Figure 11d as R1 through R5. See text for the explanation of the four rows.

own toroidal wave frequency (only one harmonic is considered here) but that the oscillation has a finite spread in both L and frequency due to damping. As a consequence, two spacecraft measuring B_ϕ with a small L separation detect common oscillations in a finite spectral band. The cross phase of the oscillations has a maximum magnitude at the center of the toroidal wave frequencies at the two spacecraft, and its sign depends on the gradient $\mathrm{d}f_\mathrm{T}/\mathrm{d}L$.

Let us now compare the model cross phase with our observations. The column labeled R1 in Figure 13 corresponds to observations made prior to ~1200 UT, well within the plasmasphere, with Van Allen Probe A located at lower L. The observed cross phase is predominantly positive at each toroidal harmonic (Figure 11c), which is consistent with Figure 13d. In region R2 (~1210 UT), there was a steep inward gradient of n_e (and ρ_eq by assumption), which causes the cross phase to become negative. In region R3 (~1230 UT), the density gradient was reduced so that $\mathrm{d}f_\mathrm{T}/\mathrm{d}L < 0$. As a consequence, the cross phase becomes positive. The spacecraft passed the apogees as they moved from region R3 to region R4, and in region R4 (~1320 UT) they encountered a steep inward density gradient again, where the cross phase is negative. As the spacecraft moved to region R5, they were back into the deeper plasmasphere. However, because Van Allen Probe B is at lower L, the cross phase is negative, opposite to that in region R1.

We can relate the measured cross phase to the radial semiwidth of field line resonance, ϵ. According to an analytical representation of B_ϕ oscillations associated with field line resonance [e.g., *Green et al.*, 1993], the cross phase θ of B_ϕ oscillations measured at two locations separated by a radial distance of ΔR_ν is given by

$$|\theta| = 2\tan^{-1}(|\Delta R_\nu|/2\epsilon), \tag{4}$$

where the cross phase is to be evaluated at $f = (f_\mathrm{A}+f_\mathrm{B})/2$, that is, the middle of the toroidal wave frequencies at point A and point B. In our case, the two frequencies are those measured by the two spacecraft, which are indistinguishable from the frequency resolution of the Fourier spectra shown in Figure 12i. We estimate the value of ϵ using the cross-phase values in the T2 and T3 bands shown in Figure 12j. For the T2 band (~8 mHz), we have $|\theta| \sim 30°$, and with $|\Delta R_\nu| \sim 200$ km, we get $\epsilon \sim 400$ km. For the T3 band (~14 mHz), we have $|\theta| \sim 60°$ and get $\epsilon \sim 200$ km.

5.4. Azimuthal Wave Number

It is evident that we need to be careful in deriving the azimuthal wave number, m, from the phase delay of B_ϕ oscillations measured by spacecraft that are separated in both L and MLT. Even a small L separation can produce a large phase delay from the field line resonance effects, and this delay may far exceed the phase delay originating from the azimuthal variation of the wave field.

Field line resonance effects were discussed by *Sarris et al.* [2013] in a study of the m number using THEMIS. To remove the ΔL-dependent part of the delay from the total phase delay measured by two THEMIS probes separated in both L and local time, Sarris et al. estimated the ΔL dependence from the latitudinal phase variation observed on the ground with multiple magnetometers. Sarris et al. noted that this method may underestimate the phase variation (and overestimate the resonance width) in space because the ionosphere smears spatial structures in the magnetosphere [*Pilipenko and Fedorov*, 1994].

Our analysis indicates that we can separate the ΔL contributions to the phase delay without relying on ground observations. The key is to select spacecraft orbits that have an L conjunction in the region of ULF wave activity. At the conjunction, the phase delay comes only from the azimuthal wave structure. As the L separation increases, the field line resonance effects make an increasingly stronger contribution to the phase delay.

We can make a reliable evaluation of the azimuthal wave number (m) using observations made at the L conjunction of two spacecraft. On the selected Van Allen Probes orbits, the conjunction occurred at 1351 UT, and we use the cross phase evaluated for 1340–1400 UT (Figures 10e and 12e) to estimate m. At the time of the conjunction, the azimuthal separation of the spacecraft (ΔR_ϕ) was 280 km. With the delay time (Δt) of magnetic field oscillations of -0.89 s determined in section 5.1, we obtain an azimuthal phase velocity of $V_\phi = -310$ km/s, where we retain the negative sign to indicate westward propagation. The corresponding azimuthal wavelength, λ_ϕ, and m are obtained using the relationship $\lambda_\phi = |V_\phi|/f$ and the definition $|m| \equiv 2\pi R_\mathrm{E} L/\lambda_\phi = 2\pi R_\mathrm{E} L f/|V_\phi|$. The numerical expressions of these for the present case are $\lambda_\phi(\mathrm{km}) = 3.1\times10^5/f(\mathrm{mHz})$ and $|m| = 0.73\times f(\mathrm{mHz})$. For $f = 25$ mHz, which is approximately the center of the band occupied by the observed ULF waves, we get $\lambda_\phi \sim 12{,}000$ km ($= 1.9\ R_\mathrm{E}$) and $|m| \sim 18$. For the observed T3 frequency of 9.0 mHz (see Figure 12d), we get $|m| \sim 7$. For the T1 and T2 frequencies of $\sim$2.1 and $\sim$5.8 mHz that are estimated using the T1/T3 and T2/T3 relationship reported by *Takahashi and Denton* [2007], we get $|m|$ values of $\sim$1.5 and $\sim$4.2, respectively. These low $|m|$ values mean that the ionospheric screening [*Hughes and Southwood*, 1976] is weak, and we expect the waves to reach the ground.

6. Mass Density Analysis

This section describes a magnetoseismic analysis [*Chi and Russell*, 2005] of mass density at Van Allen Probe A. Detection of toroidal waves by the Van Allen Probes within the plasmasphere down to $L = 2.6$ (Figure 4) allows us to estimate the plasmaspheric mass density in ways not possible in previous studies. Among the past missions, CRRES was the closest to the Van Allen Probes in terms of orbit and instrumentation, and data from that spacecraft were used to study mass density in the inner magnetosphere [e.g., *Takahashi et al.*, 2004]. However, the CRRES mass density samples covered only $L > 3$, with the majority coming from the plasma trough region ($L > 4$). In addition, the short-lived CRRES mission resulted in poor coverage of the prenoon sector, where the detection rate of toroidal waves is highest [*Takahashi and Denton*, 2007]. Ground magnetometer data are extensively used to monitor the mass density in the plasmasphere [*Menk and Waters*, 2013], but the magnetometers are geographically fixed, and paired stations are necessary to determine the toroidal wave frequencies [*Waters et al.*, 1991]. With spacecraft observations we have the advantage of continuous L shell coverage, measurements of magnetic field for comparison with the model magnetic field used in magnetoseismic techniques, and knowledge of the electron density necessary to gain information on the ion composition. We describe how the mass density can be inferred from the toroidal wave frequencies that were determined in section 3.

6.1. The Technique

The technique for mass density derivation has been described by *Takahashi et al.* [2002] with refinements made in subsequent publications [*Takahashi et al.*, 2004; *Denton et al.*, 2004]. Briefly, we numerically solve the *Singer et al.* [1981] MHD wave equation to get the relationship between the mass density and the toroidal wave frequency. In the present application of this technique to spacecraft data, we use the TS05 model [*Tsyganenko and Sitnov*, 2005] for the background magnetic field. The choice of the magnetic field

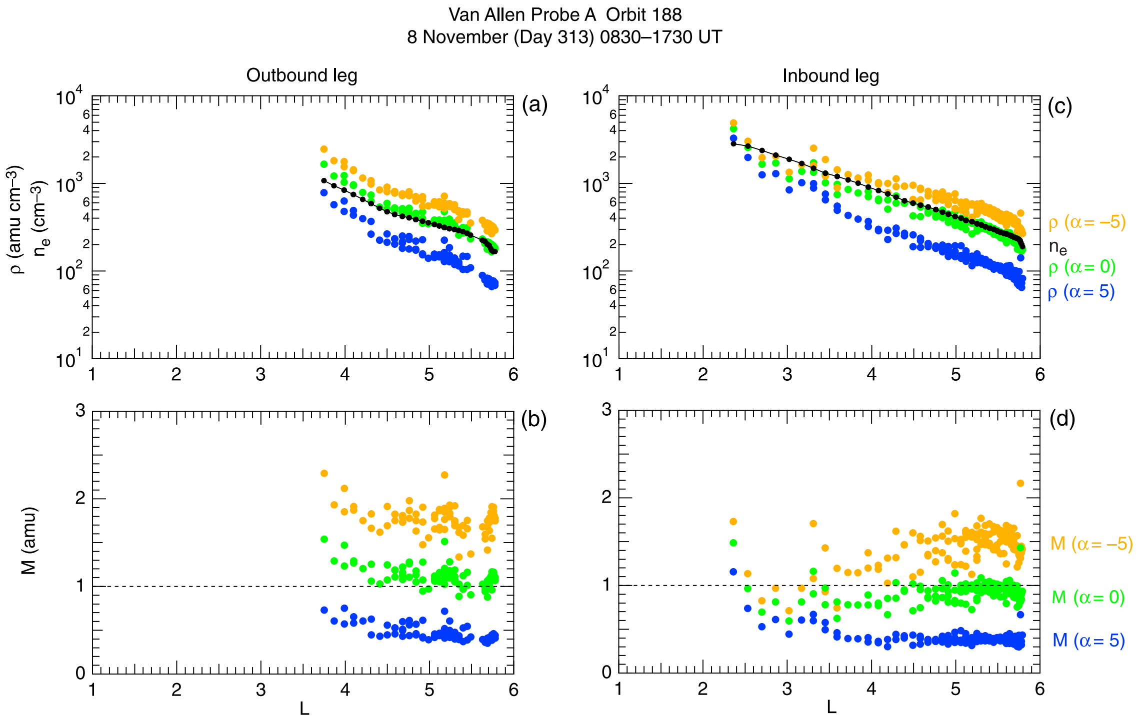

Figure 14. Mass density and related parameters at Van Allen Probe A, plotted versus dipole L, separately for the outbound and inbound legs of the orbit shown in Figure 1. (a, c) Mass density estimated from the frequencies of the observed toroidal waves, using three values of field line mass density model parameter α (orange: $\alpha = -5$, green: $\alpha = 0$, and blue: $\alpha = 5$) and the electron number density (black). (b, d) Average ion mass.

model is not very important because the geomagnetic activity was very low. The variation of the mass density ρ along the field lines is given by the power law model,

$$\rho = \rho_{\mathrm{eq}}(LR_{\mathrm{E}}/R)^{\alpha}, \tag{5}$$

where R is geocentric distance to the field line, and the exponent α is a free parameter. This density model has been widely adopted for its simplicity [*Cummings et al.*, 1969; *Orr and Matthew*, 1971; *Schulz*, 1996] and for its relevance to physical processes for particle distribution along field lines [*Angerami and Carpenter*, 1966]. If $\alpha < 0$, ρ decreases along the field line from the equator toward the ionospheric foot point. If $\alpha = 0$, ρ is constant along the field line. If $\alpha > 0$, ρ increases from the equator toward the ionospheric foot point. Perfect reflection of Alfvén waves is assumed at the ionosphere. Once ρ_{eq} is determined for a prescribed value of α, the mass density at the spacecraft is obtained using equation (5). In the present case, we have $\rho \sim \rho_{\mathrm{eq}}$, because the spacecraft were very close to the magnetic equator ($|\mathrm{MLAT}| < 5°$) in the region where toroidal waves were detected.

6.2. Estimated Mass Density and its Relation to Electron Density

Figures 14a and 14c show the L dependence of ρ and n_{e} at Van Allen Probe A, plotted separately for the inbound and outbound legs. The ρ data are derived from the toroidal wave frequencies shown in Figure 4 for three values of α. The n_{e} data are the averages in the same 15 min data windows that are used to determine the toroidal wave frequencies. Because each toroidal wave frequency sample is converted to a mass density estimate, the degree of the vertical spread of the ρ data points (for a given value of α) is a measure of the accuracy of the measurement of the frequencies as well as a measure of the goodness of our field line mass distribution model. In general, the spread is small and the ρ data points are clearly separated among the three αs shown here. In addition, ρ (for a given value of α) decreases monotonically as L increases, which is very similar to the L dependence of n_{e}. The ρ data points for $\alpha = 0$ lie particularly close to the n_{e} data points at all L. These characteristics of the estimated ρ demonstrate that our magnetoseismic technique works. Our task, then, is to choose the best value of α. In previous statistical studies [*Takahashi et al.*, 2004; *Denton et al.*, 2006; *Takahashi and Denton*, 2007], the ratio of the frequencies of different toroidal harmonics was used to determine α. In the present study, there are too few frequency samples to reliably determine the ratio, so other approaches need to be taken.

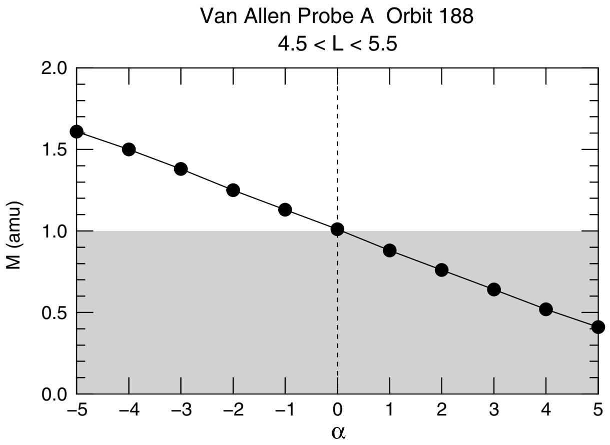

Figure 15. Median M computed from the mass density and electron density at Van Allen Probe A plotted versus α. The data cover $4.5 < L < 5.5$. The shading indicates the domain of M that is unphysical.

We can place a constraint on α by noting that there are upper and lower limits to the average magnetospheric ion mass, M, given by $M = \rho/n_e$. The mass density ρ is the sum of contributions from all ions (the electron mass is negligible), i.e., $\rho = \sum_i m_i n_i$, where m_i and n_i are the mass and number densities of the ith ion species, respectively. Charge neutrality requires $n_e = \sum_i q_i n_i$, where q_i is an integer specifying the ion charge state. In the terrestrial magnetosphere, H^+, He^+, and O^+ are the dominant ion species [e.g., *Gallagher et al.*, 2000], and we assume that the mass and number densities are accounted for by these ions, i.e., $\rho = m_{H^+}n_{H^+} + m_{He^+}n_{He^+} + m_{O^+}n_{O^+}$ and $n_e = n_{H^+} + n_{He^+} + n_{O^+}$. For a fixed value of n_e, then, the lowest ρ occurs when H^+ is the only ion constituent ($\rho = m_{H^+}n_{H^+}$, $n_e = n_{H^+}$) corresponding to $M = 1$ amu, and the highest ρ occurs when O^+ is the only constituent ($\rho = m_{O^+}n_{O^+}$, $n_e = n_{O^+}$), corresponding to $M = 16$ amu [*Takahashi et al.*, 2006]. Obviously, we need to choose a value of α so that the resulting value of ρ (along with the independently determined value of n_e) satisfies $1 \le M \le 16$ amu.

Figures 14b and 14d show the M values calculated from the parameters shown in Figures 14a and 14c, respectively. For each orbit leg, the M data points lie near $M = 1.5$, 1.0, and 0.4, for $\alpha = -5$, 0, and 5, respectively. There are deviations from these values below $L = 4$, and also some differences are seen between the outbound and inbound legs, which are discussed in section 6.3. The ~10% error for n_e described in section 2 is small and does not affect the estimation of M in any significant way. It is obvious that $\alpha = 5$ is a bad choice, because the corresponding M of 0.4 amu requires the ions to be lighter than protons.

To see the α-M relationship in more detail, we have calculated M for 11 integer values of α, from −5 to 5, and show the results in Figure 15. To generate the plot, we use data from both orbit legs covering $4.5 < L < 5.5$. The main point we learn from this figure is that we should choose $\alpha \le 0$ in order to get $M \ge 1$ amu. We believe that $\alpha \sim 0$, and, correspondingly, $M \sim 1$ amu, is a reasonable choice for the geomagnetic condition under which the waves were observed as discussed next.

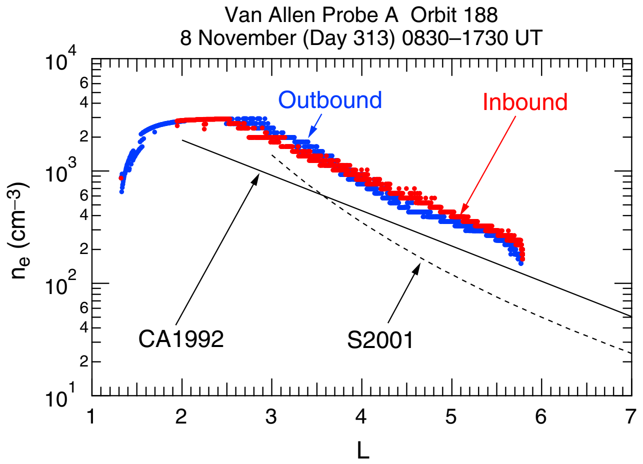

Figure 16. Electron number density at Van Allen Probe A. The straight solid line is an empirical model of saturated plasmasphere density derived by *Carpenter and Anderson* [1992]. The curved dashed line is a plasmapause density model derived by *Sheeley et al.* [2001].

Figure 16 compares the electron density at Van Allen Probe A on orbit 188 and empirical electron density models by *Carpenter and Anderson* [1992] (straight solid line labeled "CA1992") and *Sheeley et al.* [2001] (curved dashed line labeled "S2001"). The former model uses electron density measured by the ISEE spacecraft and inferred from whistler dispersion and describes the saturated plasmasphere. The latter model uses electron density measured by the CRRES spacecraft. The measured n_e at Van Allen Probe A is higher than the model n_e by a factor of ~2, implying that the plasmasphere was "supersaturated." This condition must have resulted from the prolonged geomagnetic quiescence shown in Figure 6a. The plasmapause location, inferred to be outside the Van Allen Probes apogee of $L = 5.8$, is much farther out than typical ($L \sim 4$) and is consistent with the quiet geomagnetic condition. When geomagnetic activity is low, the electron field line distribution will be close to constant according to the diffusive equilibrium theory [*Angerami and Carpenter*, 1966]. If the ion composition is dominated by H^+, we need not consider the possibility of equatorial concentration of heavy ions [*Denton et al.*, 2006], and the mass density will be also nearly constant along the field line, i.e., $\alpha \sim 0$.

6.3. Effect of Frequency Shift Caused by Spacecraft Radial Motion

The success of magnetoseismology hinges on accurate determination of wave frequencies. Toroidal wave frequencies observed from a spacecraft that cuts across L shells differ from those observed from a spacecraft that stays at a fixed L. We briefly discuss how this phenomenon affects our mass density analysis.

Observations of the frequency shift and its theoretical interpretation have been given by *Anderson et al.* [1989], who examined AMPTE/CCE data, and by *Vellante et al.* [2004] and *Heilig et al.* [2013], who examined CHAMP data. Qualitatively, if the frequency of a given toroidal harmonic is a decreasing function of L, which is usually the case except at the plasmapause, upward (downward) frequency shift occurs if the spacecraft is moving inward (outward). *Vellante et al.* [2004] treated this effect as Doppler shift. The frequency shift, if not corrected, would result in higher mass density for outbound legs and lower mass density for inbound legs.

The frequency shift appears to affect our mass density estimates shown in Figure 14. We take the $\alpha = 0$ case (green dots) as an example. On the outbound leg, M decreases from ~1.5 amu at $L = 3.7$ to ~1.0 amu at $L = 5.8$. On the inbound leg, the M samples are distributed at or slightly below 1.0 amu at all L except for a few that lie in the $M > 1.0$ domain. Because higher M means higher ρ, this difference between the orbit legs is qualitatively consistent with the frequency shift described by *Anderson et al.* [1989] and *Heilig et al.* [2013]. The frequency shift should be negligible at $L > 5$, because the radial motion of the Van Allen Probes is very slow in that region.

We note that the difference in M between the two orbit legs could be at least in part due to local time variation of field line mass distribution. For example, if we assume that field line distribution of ρ follows $\alpha \sim 1$ in the postmidnight sector (outbound leg) and $\alpha \sim -1$ in the prenoon sector (inbound leg), we can explain the difference between Figure 14b and Figure 14d without relying on the frequency shift effect. The relative importance of the frequency shift and local time dependence of field line mass distribution can be determined by statistically comparing the M values for inbound and outbound legs in the same local time sector, but such a study is beyond the scope of the present paper.

7. Summary

In summary, we have obtained the following results on ULF waves observed by the Van Allen Probes in the morning-side plasmasphere during a period of low geomagnetic activity.

7.1. Spectral Properties and Source Mechanism

The waves exhibited spectral peaks that originate from multiharmonic toroidal standing Alfvén waves. Up to the eleventh harmonics were excited with an overall spectral power enhancement in the 5–40 mHz band. The electric field intensity of the fundamental mode was weak when its frequency was below this band. The T2, T4, T6, and T8 modes are seen at 1200–1300 UT in the B_ϕ dynamic spectra (Figure 3d, see also Figure 4b) when the spacecraft were very close to the magnetic equator, the location of a magnetic field antinode of even-mode waves. However, the intensity of these even-mode waves is very low compared with that of the odd-mode waves. These observations suggest that the toroidal waves were driven by broadband source disturbances that were highly symmetric about the magnetic equator.

At the time of strong plasmaspheric ULF waves, the IMF had a small angle with respect to the Sun-Earth line. The intensity of the plasmaspheric ULF waves was correlated with the IMF cone angle—when the IMF subtended a small angle (~30°) with respect to the Sun-Earth line, the ULF amplitudes were significantly larger (by a factor of ~2) than when the cone angle was larger (~60°). Current models of upstream ULF wave generation at the quasi-parallel bow shock predict large-amplitude ULF wave generation and propagation to the magnetopause across a broad range of MLTs in such a situation [*Greenstadt et al.*, 1980], leading to a plausible source for the observed compressional waves. Current models of coupling between traveling compressional waves and toroidal standing Alfvén waves [*Lin and Wang*, 2005] then allow for excitation of the observed harmonic structure in the B_ϕ spectra. Evidence in support of this scenario has been reported at geosynchronous orbit [e.g., *Takahashi et al.*, 1984a] but not in the equatorial plasmasphere as clearly as in our present observations. In the present study, the solar wind dynamic pressure varied little as measured $\sim$260 R_E upstream of the Earth, so we argue that processes in the foreshock region (e.g., ion beam instability [*Fairfield*, 1969]) are the energy source of the plasmaspheric ULF waves.

7.2. Magnetic Field Phase Delay

Cross-spectral analysis of magnetic field data from the two spacecraft revealed different features in the compressional and azimuthal components. The compressional component exhibited a high degree of coherence regardless of satellite separation in the radial and azimuthal directions. Phase delay of the compressional oscillations between the two spacecraft is linearly related to frequency, indicating that oscillations as a whole propagate at a nearly constant fast mode velocity. The propagation of the compressional oscillation is tailward with a velocity of a few hundred kilometers per second. This velocity is close to the local fast mode velocity given by the measured magnetic field and inferred plasma mass density. Therefore, free-propagating fast mode waves can explain the phase delay. The observed E/B amplitude ratio is also consistent with fast mode velocity.

In contrast, the coherence and phase delay of the azimuthal component strongly depend on the radial separation of the spacecraft. When the two spacecraft are on the same L shell, the coherence is high and the phase delay is similar to the compressional component, both in sign and magnitude. As the radial separation increases, the coherence decreases and the phase delay increases. This behavior is explained by the radial structure of field line resonances. We were able to estimate the radial semiwidth of the resonance to be $\sim$300 km from the phase delay.

7.3. Mass Density Analysis

The toroidal waves enabled us to perform magnetoseismic analysis of the mass density over a wide range of L (2.6–5.8) within the plasmasphere and to compare the result with the electron number density. The main question was how to choose the field line model mass density parameter α. We have chosen $\alpha \sim 0$ as it is most likely, given the magnetospheric conditions during and before the event. With this choice, the mass density is constant along the field line, and the ion composition is nearly 100% H^+, which is consistent with a saturated plasmasphere. We also find evidence of the shift of toroidal frequencies induced by the radial motion of the spacecraft.

8. Conclusions

In conclusion, our study of ULF waves observed on a single orbit of the Van Allen Probes provided rich information on plasmaspheric ULF waves. The instrumentation on the spacecraft is well suited for studying the waves, and the two-spacecraft mission allows us to investigate the spatial structure and propagation of ULF waves. These unique characteristics of the mission should be valuable in addressing various questions on plasmaspheric ULF waves, for example, the L-MLT distribution of poloidal and toroidal waves, the azimuthal wave number of externally and internally driven waves, interaction of energetic particles in the ring current and radiation belt, and the mass density and ion composition in the plasmasphere.

Acknowledgments

Work at the Johns Hopkins University Applied Physics Laboratory (JHU/APL) was supported by National Science Foundation (NSF) grant AGS-1106427 and National Aeronautics and Space Administration (NASA) grants NNX13AE02G and NNX14AB97G. Work at Dartmouth College was supported by NSF grant AGS-1105790 and by NASA grants NNX10AQ60G and NNG05GJ70G. Research at the University of Iowa was supported by JHU/APL contract 921647 under NASAs Prime contract NAS5-01072. The EMFISIS data were obtained from the University of Iowa at http://emfisis.physics.uiowa.edu, the EFW data were obtained from the University of Minnesota at http://www.space.umn.edu/missions/rbspefw-home-university-of-minnesota, the solar wind and IMF data were obtained from the Goddard Space Flight Center Space Physics Data Facility OMNIWeb interface http://omniweb.gsfc.nasa.gov/ow_min.html, and the *Dst* index was obtained from the World Data Center for Geomagnetism, Kyoto, at http://wdc.kugi.kyoto-u.ac.jp/index.html.

Michael Balikhin thanks the reviewers for their assistance in evaluating this paper.

References

Allan, W., E. M. Poulter, and S. P. White (1986), Hydromagnetic wave coupling in the magnetosphere-plasmapause effects on impulse-excited resonances, *Planet. Space Sci.*, *34*(12), 1189–1220.

Anderson, B. J., M. J. Engebretson, and L. J. Zanetti (1989), Distortion effects in spacecraft observations of MHD toroidal standing waves: Theory and observations, *J. Geophys. Res.*, *94*(A10), 13,425–13,445.

Angerami, J. J., and D. L. Carpenter (1966), Whistler studies of the plasmapause in the magnetosphere: 2. Electron density and total tube electron content near the knee in the magnetospheric ionization, *J. Geophys. Res.*, *71*(3), 711–725.

Brautigam, D. H., G. P. Ginet, J. M. Albert, J. R. Wygant, D. E. Rowland, A. Ling, and J. Bass (2005), CRRES electric field power spectra and radial diffusion coefficients, *J. Geophys. Res.*, *110*, A02214, doi:10.1029/2004JA010612.

Carpenter, D. L., and R. R. Anderson (1992), An ISEE/whistler model of equatorial electron density in the magnetosphere, *J. Geophys. Res.*, *97*(A2), 1097–1108.

Chi, P. J., and C. T. Russell (2005), Travel-time magnetoseismology: Magnetospheric sounding by timing the tremor in space, *Geophys. Res. Lett.*, *32*, L18108, doi:10.1029/2005GL023441.

Chi, P. J., C. T. Russell, and J. C. Foster (2005), Density enhancement in plasmasphere-ionosphere plasma during the 2003 Halloween Superstorm: Observations along the 330th magnetic meridian in North America, *Geophys. Res. Lett.*, *32*, L03S07, doi:10.1029/2004GL021722.

Clausen, L. B. N., T. K. Yeoman, R. C. Fear, R. Behlke, E. A. Lucek, and M. J. Engebretson (2009), First simultaneous measurements of waves generated at the bow shock in the solar wind, the magnetosphere and on the ground, *Ann. Geophys.*, *27*, 357–371.

Cummings, W. D., R. J. O'Sullivan, and P. J. Coleman Jr. (1969), Standing Alfvén waves in the magnetosphere, *J. Geophys. Res.*, *74*(3), 778–793.

Dai, L., et al. (2013), Excitation of poloidal standing Alfvén waves through drift resonance wave-particle interaction, *Geophys. Res. Lett.*, *40*, 4127–4132, doi:10.1002/grl.50800.

Degeling, A. W., R. Rankin, and S. R. Elkington (2011), Convective and diffusive ULF wave driven radiation belt electron transport, *J. Geophys. Res.*, *116*, A12217, doi:10.1029/2011JA016896.

Dent, Z. C., I. R. Mann, J. Goldstein, F. M. Menk, and L. G. Ozeke (2006), Plasmaspheric depletion, refilling, and plasmapause dynamics: A coordinated ground-based and IMAGE satellite study, *J. Geophys. Res.*, *111*, A03205, doi:10.1029/2005JA011046.

Denton, R. E. (2006), Magneto-seismology using spacecraft observations, in *Magnetospheric ULF Waves: Synthesis and New Directions*, vol. 169, edited by K. Takahashi et al., pp. 307–317, AGU, Washington, D. C.

Denton, R. E., K. Takahashi, R. R. Anderson, and M. P. Wuest (2004), Magnetospheric toroidal Alfvén wave harmonics and the field line distribution of mass density, *J. Geophys. Res.*, *109*, A06202, doi:10.1029/2003JA010201.

Denton, R. E., K. Takahashi, I. A. Galkin, P. A. Nsumei, X. Huang, B. W. Reinisch, R. R. Anderson, M. K. Sleeper, and W. J. Hughes (2006), Distribution of density along magnetospheric field lines, *J. Geophys. Res.*, *111*, A04213, doi:10.1029/2005JA011414.

Engebretson, M. J., L. J. Zanetti, T. A. Potemra, and M. H. Acuña (1986), Harmonically structured ULF pulsations observed by the AMPTE CCE magnetic field experiment, *Geophys. Res. Lett.*, *13*, 905–908.

Eriksson, P. T. I., L. G. Blomberg, and K. H. Glassmeier (2006), Cluster satellite observations of mHz pulsations in the dayside magnetosphere, *Adv. Space Res.*, *38*, 1730–1737.

Fairfield, D. H. (1969), Bow shock associated waves observed in the far upstream interplanetary medium, *J. Geophys. Res.*, *74*(14), 3541–3553.

Fei, Y., A. A. Chan, S. R. Elkington, and M. J. Wiltberger (2006), Radial diffusion and MHD-particle simulations of relativistic electron transport by ULF waves in the September 1998 storm, *J. Geophys. Res.*, *111*, A12209, doi:10.1029/2005JA011211.

Gallagher, D. L., P. D. Craven, and R. H. Comfort (2000), Global core plasma model, *J. Geophys. Res.*, *105*(A8), 18,819–18,833.

Green, C. A. (1976), The longitudinal phase variation of mid-latitude Pc3–4 micropulsations, *Planet. Space Sci.*, *24*, 79–85, doi:10.1016/0032-0633(76)90064-7.

Green, A. W., E. W. Worthington, L. N. Baransky, E. N. Fedorov, N. A. Kurneva, V. A. Pilipenko, D. N. Shvetzov, A. A. Bektemirov, and G. V. Philipov (1993), Alfvén field line resonances at low latitudes ($L = 1.5$), *J. Geophys. Res.*, *98*(A9), 15,693–15,699.

Greenstadt, E. W., R. L. McPherron, and K. Takahashi (1980), Solar wind control of daytime, midperiod geomagnetic pulsations, *J. Geomagn. Geoelec.*, *32*(11), SII-89–SII-110.

Hartinger, M., M. B. Moldwin, V. Angelopoulos, K. Takahashi, H. J. Singer, R. R. Anderson, Y. Nishimura, and J. R. Wygant (2010), Pc5 wave power in the quiet-time plasmasphere and trough: CRRES observations, *Geophys. Res. Lett.*, *37*, L07107, doi:10.1029/2010GL042475.

Hasegawa, A., K. H. Tsui, and A. S. Assis (1983), A theory of long-period magnetic pulsations: 3. Local field line oscillations, *Geophys. Res. Lett.*, *10*(8), 765–767.

Heilig, B., H. Lühr, and M. Rother (2007), Comprehensive study of ULF upstream waves observed in the topside ionosphere by CHAMP and on the ground, *Ann. Geophys.*, *25*, 737–754.

Heilig, B., P. R. Sutcliffe, D. C. Ndiitwani, and A. B. Collier (2013), Statistical study of geomagnetic field line resonances observed by CHAMP and on the ground, *J. Geophys. Res. Space Physics*, *118*, 1934–1947, doi:10.1002/jgra.50215.

Hughes, W. J., and D. J. Southwood (1976), The screening of micropulsation signals by the atmosphere and ionosphere, *J. Geophys. Res.*, *81*, 3234–3247.

Junginger, H., G. Geiger, G. Haerendel, F. Melzner, E. Amata, and B. Higel (1984), A statistical study of dayside magnetospheric electric field fluctuations with periods between 150 and 600 s, *J. Geophys. Res.*, *89*(A7), 5495–5505.

Kletzing, C. A., et al. (2013), The Electric and Magnetic Field Instrument Suite and Integrated Science (EMFISIS) on RBSP, *Space Sci. Rev.*, *179*, 127–181, doi:10.1007/s11214-013-9993-6.

Lee, D. H. (1996), Dynamics of MHD wave propagation in the low-latitude magnetosphere, *J. Geophys. Res.*, *101*(A7), 15,371–15,386.

Lee, D. H. (1998), On the generation mechanism of Pi2 pulsations in the magnetosphere, *Geophys. Res. Lett.*, *25*(5), 583–586.

Lee, D. H., and R. L. Lysak (1989), ULF wave coupling in the dipole model: The impulsive excitation, *J. Geophys. Res.*, *94*, 17,097–17,103.

Lin, Y., and X. Y. Wang (2005), Three-dimensional global hybrid simulation of dayside dynamics associated with the quasi-parallel bow shock, *J. Geophys. Res.*, *110*, A12216, doi:10.1029/2005JA011243.

Liu, W., J. B. Cao, X. Li, T. E. Sarris, Q.-G. Zong, M. Hartinger, K. Takahashi, H. Zhang, Q. Q. Shi, and V. Angelopoulos (2013), Poloidal ULF wave observed in the plasmasphere boundary layer, *J. Geophys. Res. Space Physics*, *118*, 4298–4307, doi:10.1002/jgra.50427.

Mauk, B. H., N. J. Fox, S. G. Kanekal, R. L. Kessel, D. G. Sibeck, and A. Ukhorskiy (2013), Science objectives and rationale for the Radiation Belt Storm Probes mission, *Space Sci. Rev.*, *179*(1–4), 3–27, doi:10.1007/s11214-012-9908-y.

Menk, F. W., and C. L. Waters (2013), *Magnetoseismology*, 251 pp., Wiley-VCH, Weinheim, Germany.

Orr, D., and J. A. D. Matthew (1971), The variation of geomagnetic micropulsation periods with latitude and the plasmapause, *Planet. Space Sci.*, *19*, 897–905.

Pilipenko, V. A., and E. N. Fedorov (1994), Magnetotelluric sounding of the crust and hydrodynamic monitoring of the magnetosphere with the use of ULF waves, in *Solar Wind Sources of Magnetospheric Ultra-Low-Frequency Waves, Geophys. Monogr. Ser*, vol. 81, edited by M. J. Engebretson, K. Takahashi, and M. Scholer, pp. 283–292, AGU, Washington, D. C.

Pilipenko, V. A., M. Vellante, and E. N. Fedorov (2000), Distortion of the ULF wave spatial structure upon transmission through the ionosphere, *J. Geophys. Res.*, *105*(A9), 21,225–21,236.

Sarris, T. E., et al. (2009), Characterization of ULF pulsations by THEMIS, *Geophys. Res. Lett.*, *36*, L04104, doi:10.1029/2008GL036732.

Sarris, T. E., X. Li, W. Liu, E. Argyriadis, A. Boudouridis, and R. Ergun (2013), Mode number calculations of ULF field-line resonances using ground magnetometers and THEMIS measurements, *J. Geophys. Res. Space Physics*, *118*, 6986–6997, doi:10.1002/2012JA018307.

Schulz, M. (1996), Eigenfrequencies of geomagnetic field lines and implications for plasma-density modeling, *J. Geophys. Res.*, *101*, 17,385–17,397.

Sheeley, B. W., M. B. Moldwin, H. K. Rassoul, and R. R. Anderson (2001), An empirical plasmasphere and trough density model: CRRES observations, *J. Geophys. Res.*, *106*(A11), 25,631–25,641.

Singer, H. J., D. J. Southwood, R. J. Walker, and M. G. Kivelson (1981), Alfvén wave resonances in a realistic magnetospheric magnetic field geometry, *J. Geophys. Res.*, *86*(A6), 4589–4596.

Sugiura, M., and C. R. Wilson (1964), Oscillation of the geomagnetic field lines and associated magnetic perturbations at conjugate points, *J. Geophys. Res.*, *69*(7), 1211–1216.

Takahashi, K., and B. J. Anderson (1992), Distribution of ULF energy ($f < 80$ mHz) in the inner magnetosphere: A statistical analysis of AMPTE CCE magnetic field data, *J. Geophys. Res.*, *97*(A7), 10,751–10,773.

Takahashi, K., and R. E. Denton (2007), Magnetospheric seismology using multiharmonic toroidal waves observed at geosynchronous orbit, *J. Geophys. Res.*, *112*, A05204, doi:10.1029/2006JA011709.

Takahashi, K., and R. L. McPherron (1982), Harmonic structure of Pc3–4 pulsations, *J. Geophys. Res.*, *87*, 1504–1516.

Takahashi, K., R. L. McPherron, and T. Terasawa (1984a), Dependence of the spectrum of Pc3–4 pulsations on the interplanetary magnetic field, *J. Geophys. Res.*, *89*, 2770–2780.

Takahashi, K., R. L. McPherron, and W. J. Hughes (1984b), Multispacecraft observations of the harmonic structure of Pc3–4 magnetic pulsations, *J. Geophys. Res.*, *89*, 6758–6774.

Takahashi, K., P. R. Higbie, and D. N. Baker (1985), Azimuthal propagation and frequency characteristic of compressional Pc5 waves observed at geostationary orbit, *J. Geophys. Res.*, *90*(A2), 1473–1485.

Takahashi, K., B. J. Anderson, and R. J. Strangeway (1990), AMPTE CCE observations of Pc3-4 pulsations at L = 2–6, *J. Geophys. Res.*, *95*(A10), 17,179–17,186.

Takahashi, K., et al. (1994), GEOTAIL observation of magnetosonic Pc3 waves in the dayside magnetosphere, *Geophys. Res. Lett.*, *21*, 2899–2902.

Takahashi, K., R. E. Denton, and D. Gallagher (2002), Toroidal wave frequency at L = 6–10: Active magnetospheric particle tracer explorers/CCE observations and comparison with theoretical model, *J. Geophys. Res.*, *107*(A2), 1020, doi:10.1029/2001JA000197.

Takahashi, K., R. E. Denton, R. R. Anderson, and W. J. Hughes (2004), Frequencies of standing Alfvén wave harmonics and their implication for plasma mass distribution along geomagnetic field lines: Statistical analysis of CRRES data, *J. Geophys. Res.*, *109*, A08202, doi:10.1029/2003JA010345.

Takahashi, K., R. E. Denton, R. R. Anderson, and W. J. Hughes (2006), Mass density inferred from toroidal wave frequencies and its comparison to electron density, *J. Geophys. Res.*, *111*, A01201, doi:10.1029/2005JA011286.

Takahashi, K., R. E. Denton, S. Ohtani, W. J. Hughes, and R. R. Anderson (2008), Ion composition in the plasma trough and plasma plume derived from a combined release and radiation effects satellite magnetoseismic study, *J. Geophys. Res.*, *113*, A12203, doi:10.1029/2008JA013248.

Takahashi, K., D. Berube, D.-H. Lee, J. Goldstein, H. J. Singer, F. Honary, and M. B. Moldwin (2009), Possible evidence of virtual resonance in the dayside magnetosphere, *J. Geophys. Res.*, *114*, A05206, doi:10.1029/2008JA013898.

Takahashi, K., et al. (2010a), Multipoint observation of fast mode waves trapped in the dayside plasmasphere, *J. Geophys. Res.*, *115*, A12247, doi:10.1029/2010JA015956.

Takahashi, K., R. E. Denton, and H. J. Singer (2010b), Solar cycle variation of geosynchronous plasma mass density derived from the frequency of standing Alfvén waves, *J. Geophys. Res.*, *115*, A07207, doi:10.1029/2009JA015243.

Tamao, T. (1964), The structure of three-dimensional hydromagnetic waves in a uniform cold plasma, *J. Geomagn. Geoelec.*, *16*, 89–114.

Tamao, T. (1978), Coupling modes of hydromagnetic oscillations in non-uniform, finite pressure plasmas: Two-fluids model, *Planet. Space Sci.*, *26*, 1141–1148.

Troitskaya, V. A. (1994), Discoveries of sources of Pc 2-4 waves—A review of research in the former USSR, in *Solar Wind Sources of Magnetospheric Ultra-Low-Frequency Waves, Geophys. Monogr. Ser.*, vol. 81, edited by M. J. Engebreston, K. Takahashi, and M. Scholer, pp. 45–54, AGU, Washington, D. C.

Troitskaya, V. A., and O. V. Bolshakova (1988), Diagnostics of the magnetosphere using multipoint measurements of ULF waves, *Adv. Space Res.*, *8*(9–10), 413–425.

Troitskaya, V. A., T. A. Plyasova-Bakounina, and A. V. Gul'yel'mi (1971), Relationship between Pc2-4 pulsations and the interplanetary magnetic field, *Dokl. Akad. Nauk*, *197*, 1312–1314.

Tsyganenko, N. A. (1989), A magnetospheric magnetic field model with a warped tail current sheet, *Planet. Space Sci.*, *37*, 5–20.

Tsyganenko, N. A., and M. I. Sitnov (2005), Modeling the dynamics of the inner magnetosphere during strong geomagnetic storms, *J. Geophys. Res.*, *110*, A03208, doi:10.1029/2004JA010798.

Vellante, M., U. Villante, M. De Lauretis, and G. Barchi (1996), Solar cycle variation of the dominant frequencies of Pc3 geomagnetic pulsations at L = 1.6, *Geophys. Res. Lett.*, *23*(12), 1505–1508.

Vellante, M., et al. (2004), Ground/satellite signatures of field line resonance: A test of theoretical predictions, *J. Geophys. Res.*, *109*, A06210, doi:10.1029/2004JA010392.

Villante, U., P. Francia, M. Vellante, P. D. Giuseppe, A. Nubile, and M. Piersanti (2007), Long-period oscillations at discrete frequencies: A comparative analysis of ground, magnetospheric, and interplanetary observations, *J. Geophys. Res.*, *112*, A04210, doi:10.1029/2006JA011896.

Walker, A. D. M., R. A. Greenwald, W. F. Stuart, and C. A. Green (1979), Stare auroral radar observations of Pc5 geomagnetic pulsations, *J. Geophys. Res.*, *84*(A7), 3373–3388.

Waters, C. L., F. W. Menk, and B. J. Fraser (1991), The resonance structure of low latitude Pc3 geomagnetic pulsations, *Geophys. Res. Lett.*, *18*(12), 2293–2296.

Waters, C. L., F. W. Menk, M. F. Thomsen, C. Foster, and F. R. Fenrich (2006), Remote sensing the magnetosphere using ground-based observations of ULF waves, in *Magnetospheric ULF Waves, Geophys. Monogr. Ser.*, vol. 169, edited by K. Takahashi et al., pp. 319–340, AGU, Washington, D. C.

Wolfe, A., L. J. Lanzerotti, and C. G. Maclennan (1980), Dependence of hydromagnetic energy spectra on solar wind velocity and interplanetary magnetic field direction, *J. Geophys. Res.*, *85*(A1), 114–118, doi:10.1029/JA085iA01p00114.

Wygant, J. R., et al. (2013), The electric field and waves instruments on the radiation belt storm probes mission, *Space Sci. Rev.*, *179*, 183–220, doi:10.1007/s11214-013-0013-7.

Yumoto, K., T. Saito, B. Tsurutani, E. Smith, and S.-I. Akasofu (1984), Relationship between the IMF magnitude and Pc 3 magnetic pulsations in the magnetosphere, *J. Geophys. Res.*, *89*(A11), 9731–9740.